

Optical, Thermal and Crystallization Characteristics of Metallic Glasses

by

Ceren Uzun, M.S.

A Dissertation

In

Physics

Submitted to the Graduate Faculty
of Texas Tech University in
Partial Fulfillment of
the Requirements for
the Degree of

DOCTOR OF PHILOSOPHY

Approved

Ayrton A. Bernussi
Chair of Committee

Golden Kumar

Luis Grave de Peralta

Mahdi Sanati

Mark Sheridan
Dean of the Graduate School

May 2020

©2020, Ceren Uzun

ACKNOWLEDGEMENTS

“No man is an island...” so, I would like to take this opportunity to express my gratitude to the many amazing people who made this work possible. I am extremely grateful to my advisor and mentor, **Dr. Ayrton Bernussi** who has been nothing less than a father to me, not only for his academic support and valuable guidance throughout my studies at the TTU Nanotech Center but also for enabling a personal relationship that made me feel welcomed, respected, and valued at all times. Many thanks to **Dr. Golden Kumar** for sharing his vast knowledge on metallic glasses with me and his students **Niloofer Kahler**, **Zhonglue Hu**, and **Chandra Sekhar Meduri** for spending endless hours in the laboratory for fabricating the metallic glass samples that I desperately needed. I am indebted to **Dr. Luis Grave de Peralta** for lending me various equipment and supporting me as a part of my committee member. I would like to acknowledge another committee member **Dr. Mahdi Sanati** for the valuable insight he has added to this work and for being the best teacher that I have ever had.

Special thanks to **Dr. Vladimir Kuryatkov** for sharing his incredible technical knowledge and skills with me. I am thankful for my **TTU Physics and Astronomy Department and the Nanotech Center** family and colleagues for their kindness, helpfulness, and positive attitude over the years.

Thank you, my forever friends **Victor Siller** and **Shivakumar Surendranath**, for being there for me in your own unique ways.

Many thanks to my family on this side of the world, my spouse **Raymond F. Russell** and my babies **Mancha** and **Zeytin**, for keeping me sane, grounded and loved in good days and bad days when things got overwhelmingly complicated.

I would like to acknowledge my extreme luck of having **Berk Uzun**, **Fulya Uzun**, and **Mert Uzun** as my siblings, I love you guys to the moon and back.

Mürvet Sakik, thank you for being my mom and my best friend. You are the pillar of my being, and the source of resilience, compassion and inspiration in my life.

Finally, I would like to dedicate this work to the loving memory of my late father, **Mehmet Uzun**, who would have turned 71 today. I will forever be proud to have inherited the love of science from you. Happy birthday, dad.

TABLE OF CONTENTS

ACKNOWLEDGEMENTS.....	ii
ABSTRACT.....	v
LIST OF TABLES.....	vii
LIST OF FIGURES.....	viii
1. INTRODUCTION.....	1
2. LOW REFLECTANCE OF METALLIC GLASS NANOWIRE ARRAYS.....	5
2.1 Introduction.....	5
2.2 Experimental Details of Integrated Diffuse Reflectance Measurements.....	5
2.3 Results and Discussion.....	7
2.3.1 Effects of Nanowire Aspect Ratio on Integrated Diffuse Reflectance.....	7
2.3.2 Wavelength Dependence of Integrated Diffuse Reflectance.....	9
2.3.3 Rigorous Coupled Wave Analysis Simulations of Diffuse Reflectance...	10
2.4 Enhancing Reflectance: Bundling Effect of Vertically Aligned Nanowires.....	12
2.5 Conclusions.....	15
3. SPECKLE IMAGE ANALYSIS OF METALLIC GLASS SCATTERERS VIA CLASSIFIER ALGORITHM.....	17
3.1 Introduction.....	17
3.2 Experimental Details.....	18
3.3 Results and Discussion.....	20
3.3.1 Selection of Parameters.....	20
3.3.2 Selection of Classifier Algorithm.....	21
3.3.3 Identifying a Sample Using Speckle Images.....	22
3.4 Conclusions.....	24
4. PHOTO-INDUCED HEAT LOCALIZATION ON NANOSTRUCTURED METALLIC GLASSES.....	25
4.1 Introduction.....	25
4.2 Experimental Details.....	25

4.3	Results and Discussion.....	28
4.3.1	Heat Localization Effect.....	28
4.3.2	Excitation Power Dependence of Induced Temperature.....	29
4.4	An Application of Heat Conversion: Infrared Steganography, Tagging, and Tracking.....	30
4.5	Conclusions.....	32
5.	PHOTO-INDUCED HEAT CONVERSION ENHANCEMENT OF METALLIC GLASS NANOWIRE ARRAYS.....	33
5.1	Introduction.....	33
5.2	Experimental Details.....	33
5.3	Results and Discussion.....	35
5.3.1	Effects of Base Thickness and Aspect Ratio of Nanowires on Absorption.....	35
5.3.2	Effects of Base Thickness and Aspect Ratio of Nanowires on Photo-induced Temperatures.....	36
5.3.3	Finite Element Analysis of Heat Transfer Through Metallic Glass Nanowires.....	39
5.3.4	Effects of the Phase Transition on Photo-induced Temperatures.....	41
5.4	An Application of Heat Conversion: Optical Ignition of Al+CuO Thermite Powder.....	43
5.5	Conclusions.....	45
6.	DIELECTRIC PROPERTIES OF CRYSTALLINE AND AMORPHOUS METALLIC GLASSES.....	47
6.1	Introduction.....	47
6.2	Experimental Details.....	47
6.2.1	Sample Preparation and Crystallization.....	47
6.2.2	Spectroscopic Ellipsometry.....	48
6.3	Results and Discussion.....	50
6.4	Conclusions.....	53

7. CONCLUSIONS	54
7.1 List of Publications	56
REFERENCES	57

ABSTRACT

Materials with large photo-thermal energy conversion efficiency are essential for a wide variety of applications spanning from medicine to renewable energy.

Photoexcitation is an effective approach to generate controlled and localized heat at relatively low optical powers. However, lateral heat diffusion to the surrounding illuminated areas accompanied by low photo-thermal energy conversion efficiency remains a challenge for metallic surfaces. Surface nanoengineering has proven to be a successful approach to further absorption and heat generation.

In this dissertation, we investigate the optical, thermal and crystallization properties of arrays of metallic glass nanowires. Integrated diffuse reflectance measurements and rigorous coupled wave analysis simulations at different angles of incidence and different wavelengths were used to characterize the absorption properties of metallic glass nanowires with different length-to-diameter aspect ratios. Our measurements and simulations revealed the importance of the nanowire profile (vertically aligned or bundled) in the reflectance of nanopatterned metallic glasses. Furthermore, the scattering properties of metallic glass nanowires were investigated using speckle imaging. Statistical analysis of the speckle images obtained from samples with different aspect ratios, amorphicity and crystallinity revealed distinct features of these scatterers. These features are then used in various machine learning algorithms for classification of new speckle images. High accuracy of the classifier algorithms enabled a speckle analysis-based method for characterization of the topology and the structural state of metallic glasses. We further show that pronounced spatial heat localization and high temperatures can be achieved with arrays of amorphous metallic glass nanowires whose geometry can be readily tailored through thermoplastic molding. Thermography measurements revealed marked temperature contrast between illuminated and non-illuminated areas even under low optical power excitation conditions. This attribute allowed for generating legible photo-induced thermal patterns on textured metallic glass surfaces. We have also demonstrated that the optical absorption and coupled heat conversion in the near infrared can be enhanced by tailoring the metallic glass nanowire topology. Infrared thermography measurements and heat transport simulations reveal that the photo-induced

temperature rise can be amplified by increasing the length of nanowires and decreasing the thickness of the supporting substrate. Temperatures above 500°C can be rapidly achieved to induce a controlled phase transformation from amorphous to crystalline state in metallic glass nanowires while maintaining their geometrical integrity. We utilized the photo-induced temperature rise of metallic glass nanowires in optical ignition application as demonstrated by the ignition example of thermite powder. We further explore the effects of structural state (amorphous and crystalline) on the optical characteristics of the metallic glass nanowires. The optical constants of unpatterned amorphous and crystalline samples were measured using spectroscopic ellipsometry. Thus, an optical characterization method based on ellipsometry was introduced to verify the crystallinity of metallic glasses.

LIST OF TABLES

3.1	Average figure of merit ranking of the statistical parameters used in the speckle image classification obtained from different algorithms.....	21
5.1	Labeling scheme and description of Pt-MG samples used in this study. ⁴³	34

LIST OF FIGURES

1.1	(a) SEM image of the patterned Pt-MG ²⁷ and (b) and (c) optical images of the patterned Pt-MG and unpatterned (flat) Pt-MG samples, respectively.....	2
1.2	Schematic diagram of thermoplastic embossing scheme of metallic glass wafer onto the AAO template. ²⁸	3
2.1	Schematic illustration of the set up used in the integrated diffuse reflectance experiments: BS: beam splitter, LPL: linear polarizer, $\lambda/2$: half-wave plate.....	7
2.2	The angular dependence of diffuse reflectance measured and simulated for patterned (HAR and LAR) and flat (F) samples at $\lambda=980\text{nm}$	8
2.3	Experimental and simulated diffuse reflectance of Pt-MG nanowires with $l/d\sim 10$ aspect ratio at $\lambda = 532\text{nm}$, 980nm , and 1560nm and incident angle $\theta_i = 10^\circ$	10
2.4	Nanowire design layout of (a) the top view (b) 3D-view for a sample, parameters $l\sim 1000$, $d\sim 100\text{nm}$, and $p\sim 250\text{nm}$ with 50% variation.....	11
2.5	SEM image of the patterned Pt-MG (a) in its vertical state, and (b) in its bundled state. ²⁸	13
2.6	The angular dependence of measured and simulated diffuse reflectance of vertically aligned and bundled samples at $\lambda=1560\text{ nm}$. ²⁸	14
2.7	(a) Simulated angular dependence of diffuse reflection at $\lambda = 1560\text{nm}$ for Pt-MG nanowires with different bundling profiles. (b-e) CAD profiles of the simulated structure as a function of extent of bundling.....	15
3.1	Schematic illustration of the main tasks used to perform the classification of speckle images.....	18
3.2	Speckle images of samples with different topologies and structural states corresponding to each class.....	19

3.3	(a) Schematic illustration of the set up used in the speckle image acquisition experiments (b) a representative speckle image of the Pt-MG nanowire sample with aspect ratio $l/d \sim 12$	20
3.4	Performance evaluation of multi-class functions in Weka using 10-fold cross validation on the training data.....	22
3.5	(a) Classifier flowchart (b) rate of instances correctly classified by SMO, IBk, Logistic, and Naïve Bayes classifier algorithms, respectively.....	23
4.1	(a) and (c) SEM images and (b) and (d) optical images of the patterned Pt-MG and BAA samples, respectively. ⁴²	26
4.2	Measured angular dependence of absorption for patterned Pt-MG and BAA samples at $\lambda=980\text{nm}$. ⁴²	27
4.3	Schematic illustration of the set up used in the photo-thermal experiments. ⁴²	28
4.4	Thermal images of (a) patterned Pt-MG and (b) BAA samples at $P=1\text{ W/mm}^2$. (c) Horizontal temperature line profiles of the thermal images shown in (a) and (b). The laser spot size (black ellipse) is also illustrated in (a) and (b). ⁴²	29
4.5	Horizontal temperature line profiles for a patterned Pt-MG sample at different laser power densities. The inset shows the maximum temperature for each laser excitation power density. ⁴²	30
4.6	Thermal images of the several Lissajous patterns configured onto patterned Pt-MG. $A_1=A_2=0.2\text{ V}$ (a) $m=n=1$, $\varepsilon=\pi/2$, $P=2.3\text{ W/mm}^2$; (b) $m=2\ n=3$, $\varepsilon=\pi/4$, $P=2.5\text{ W/mm}^2$; (c) $m=1\ n=4$, $\varepsilon=3\pi/8$, $P=2.3\text{ W/mm}^2$ (d) $m=1\ n=2$, $\varepsilon=0$, $P=2.2\text{ W/mm}^2$. ⁴²	31
5.1	Schematic illustration of sample geometry (not to scale) and SEM images of two Pt-MG samples patterned with nanowires of different lengths. ⁴³	35
5.2	Measured absorption angular dependence of patterned (HAR-t ₁ , LAR-t ₁ , HAR-t ₂ , and LAR-t ₂) and flat (F-t ₁ and F-t ₂) Pt-MG samples at $\lambda = 980\text{ nm}$. ⁴³	36

5.3	Thermal images of (a) HAR-t ₁ and (b) F-t ₁ Pt-MG samples obtained at identical laser power density of $\sim 2.8 \text{ W/mm}^2$. ⁴³	37
5.4	Measured and simulated maximum photo-induced temperature rise for patterned (HAR-t ₁ , LAR-t ₁ , HAR-t ₂ , and LAR-t ₂) and unpatterned (F-t ₁ and F-t ₂) Pt-MG samples at different laser excitation power densities. ⁴³	38
5.5	(a) Schematic illustration of single nanowire unit cell geometry (not to scale) used in the simulations. Simulated temperature distribution of single nanowire unit cell with $l/d=10$ and $t=50 \text{ }\mu\text{m}$ (HAR-t ₁) at power density $\sim 2.8 \text{ W/mm}^2$ (b) from the top view and (c) from the bottom view. ⁴³	41
5.6	(a) Measured maximum photo-induced temperature rise on patterned amorphous and crystalline Pt-MG (VHR-t) samples at different laser excitation power densities. SEM image of (b) the as-prepared crystalline sample (VHR-t Crystalline), and (c) the sample crystallized by photo-induced heating (VHR-t Amorphous Exp #2). ⁴³	43
5.7	(a) SEM images of nano-patterned Pt-MG in the as-prepared state, after coating with thermite mixture, and after laser ignition of thermite. (b) Schematic illustration of laser ignition setup and still images captured at different times from the video recording obtained with a laser power density $\sim 12 \text{ W/mm}^2$. ⁴³	45
6.1	Time-Temperature-Transition diagram for Pt _{57.5} Cu _{14.7} Ni _{5.3} P _{22.5} in the super cooled liquid region. Open and closed squares represent the onset and end of crystallization, respectively. (Adapted from Reference [44])	48
6.2	Schematic representation of the elliptical polarization state showing the electric field amplitudes (E_{rp} and E_{rs}) and the ellipsometry angles Δ and Ψ	49
6.3	XRD patterns of the Pt-MG in (a) the crystalline state, and (b) the amorphous state, respectively. (Adapted from Reference [56]).	51
6.4	Measured and fitted I_s and I_c parameters as a function of wavelength for Pt-MG sample in (a) the amorphous state, and (b) the crystalline state.	52
6.5	Index of refractions (n) and extinction coefficients (k) as a function of wavelength for amorphous and crystalline Pt-MG.	52

CHAPTER 1

INTRODUCTION

Artificially engineered materials with nearly unit absorption over a broad range of frequencies and incidence angles are essential in a myriad of applications including stealth, solar-thermal-electrical conversion, solar heaters, photovoltaics, and material processing.¹⁻⁶ These applications typically involve highly absorbing nanostructured materials which effectively convert light into heat at desirable excitation wavelengths. Photo-thermal energy conversion is of particular interest for clean and renewable energy applications. The efficiency of photo-thermal energy conversion depends on the material type (metal, semiconductor, or insulator), surface topology, and frequency dependent absorption. An effective approach to achieve high absorption involves surface nanotexturing. This has been demonstrated for nanostructured metals, insulators, amorphous and crystalline semiconductors, and carbon nanotubes.⁷⁻¹⁰ However, depending on the surface topology, lateral heat dissipation to the surrounding illuminated areas may limit photo-thermal energy conversion. Vertically aligned nanowires with high length-to-diameter aspect ratios exhibit large surface areas and lower effective thermal conductivity, and thus, reduced lateral heat diffusion when compared to their bulk counterparts.^{11,12} Vertically aligned single-walled and multi-walled carbon nanotube (CNT) arrays have been extensively studied for photo-thermal-electric conversion applications due to their enhanced thermal conductivity,¹³ light trapping efficiency,^{14,15} and heat localization effects.¹⁶ Photo-thermal energy conversion has also been demonstrated using semiconducting nanowire arrays (NWA) of Si and GaAs.^{17,18} High optical absorption and thermal conductivity of metallic (e.g. Bi and Cu) NWAs have been utilized for thermo-electric power generation applications.^{19,20} Although different fabrication techniques such as electrospinning,²¹ vapor-liquid-solid (VLS),²² and catalytic growth²³ have been developed to synthesize nanowires of diverse materials, the inability to produce large NWAs and limited control over nanowire dimensions remain challenging. These manufacturing issues can be mitigated by using thermoplastic materials which can be directly embossed into nanostructures over wafer-scale areas. Polymeric materials are not suitable for photo-thermal applications because of poor

optical absorption and low melting temperature. In contrast, metallic glasses (MGs) are ideal candidates for photo-thermal applications because of their metal-like optical and thermal properties and polymer-like shaping capability. MGs exhibit high mechanical strength, high corrosion and wear resistance, and are known to be thermally stable up to their glass transition temperatures. Like thermoplastics, MGs can be molded into nanostructures above their glass transition temperature which is comparable to plastics for some MGs.²⁴ The ability to easily reshape MGs into various profiles such as vertically aligned or bundled, smooth or rough, amorphous or crystalline, and convex or concave tip shaped nanowires is attractive for photo-thermal applications.^{25,26} However, the use of nanopatterned MGs for photo-thermal energy conversion applications has not been explored thus far. To achieve this, we combine various optical and thermal measurements and simulations using unpatterned and patterned MG samples with different topologies, profiles, and structural states in this study.

A representative scanning electron microscope (SEM) image of the MG ($\text{Pt}_{57.5}\text{Cu}_{14.7}\text{Ni}_{5.3}\text{P}_{22.5}$) nanowire topology patterned via thermoplastic molding investigated in this study is shown in Figure 1.1 (a).²⁷ Figures 1.1 (b) and (c) show optical images of patterned and unpatterned (or flat) amorphous platinum-based metallic glass (Pt-MG) samples, respectively. Nanopatterned surface exhibits a lower reflectance compared to its mirror-like unpatterned counterpart as evident from the figure.

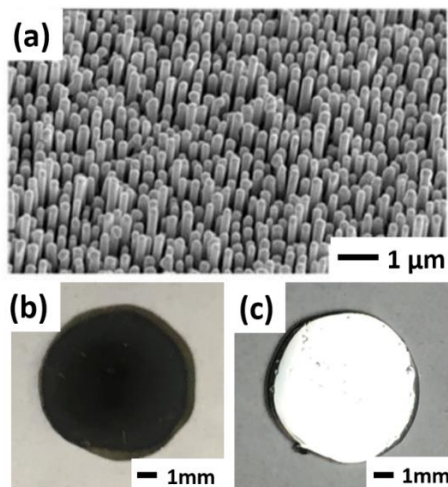


FIG. 1.1 (a) SEM image of the patterned Pt-MG²⁷ and (b) and (c) optical images of the patterned Pt-MG and unpatterned (flat) Pt-MG samples, respectively.

A schematic illustration of the thermoplastic embossing process used for patterning metallic glass nanowires is shown in Figure 1.2. Unpatterned and patterned discs of Pt-MG investigated in this study were synthesized by water quenching and nanomoulding as reported previously.^{24,28} The metallic glass was heated above its glass transition temperature ($\sim 230^\circ\text{C}$) and embossed into the nanoporous anodized aluminum oxide (AAO) templates. The AAO template was etched away using a KOH solution. The patterned metallic glass was rinsed in deionized water (DI-water) and dried under air flow. Nanopatterned samples with different aspect ratios (*length/diameter*) were fabricated by varying the embossing pressure. While samples with lower aspect ratios retain their vertically aligned nanowire topology, higher aspect ratio samples ($l/d > 20$) tend to form into bundles as the aspect ratio increases.²⁸

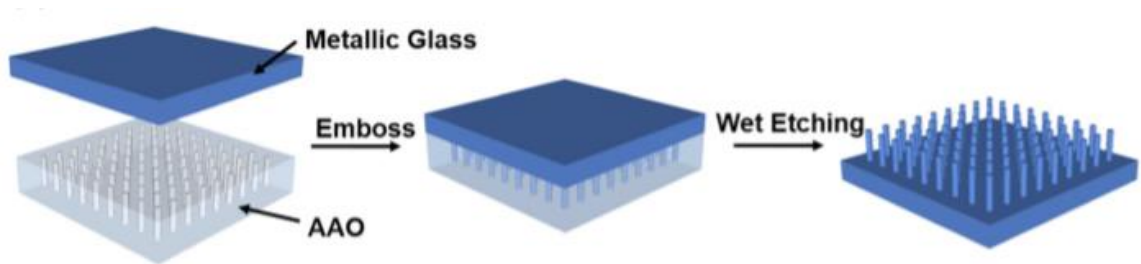


FIG. 1.2 Schematic illustration of the thermoplastic embossing process of metallic glass using an AAO template.²⁸

In this dissertation, we investigate the optical, thermal and phase transition characteristics of metallic glass nanowire arrays for various photo-thermal applications. In Chapter 1, we present an overview of materials used in photo-thermal energy conversion applications and underlines our motivation to use metallic glasses. In Chapter 2, we report the experimental and simulated results on the low diffuse reflectance of metallic glass nanowire arrays, and we demonstrate the enhancement of low reflectance by bundling the nanowires. We also study the scattering properties of metallic glasses with different surface topologies and structural states using statistical speckle image analysis based on a machine learning algorithm in Chapter 3. The heat localization and the potential

applications of this effect in steganography, IR tagging, and tracking is discussed in Chapter 4. In Chapter 5, we extend our discussion of photo-thermal behavior of the metallic glass nanowires to the effects of the topology and structural state of the nanowires with both experiments and heat transfer simulations. We also demonstrate laser ignition of thermite powder at significantly lower laser flux using metallic glass nanowires. In Chapter 6, we investigate the dielectric properties of amorphous and crystalline metallic glasses using spectroscopic ellipsometry. Conclusions of this dissertation and a list of my publications on these subjects are given in Chapter 7.

CHAPTER 2

LOW REFLECTANCE OF METALLIC GLASS NANOWIRE ARRAYS

2.1 Introduction

Effective conversion of light into heat is essential in photo-thermal energy conversion applications. This can only be achieved with materials that exhibit high absorption characteristics. We previously demonstrated that low reflectance (<2%) over a wide range of incident angles, in the visible frequency range, can be achieved with arrays of MG nanowires.²⁷ Here, we investigate the effects of the aspect ratio of nanowires on the diffuse reflectance and further explore the illumination wavelength dependence of the diffuse reflectance in the near infrared and compare our findings with rigorous coupled wave analysis (RCWA) simulations.

Our results revealed the significance of aspect ratio of nanowires in achieving low reflectance. We determined that the diffuse reflectance of MG nanowire arrays increase as the wavelength of the illumination is increased. We showed that it is possible to further reduce the reflectance by bundling the MG NWAs in controllable manner. All measurements of diffuse reflectance were verified by RCWA simulations.

2.2 Experimental Details

Details about the synthesis and the patterning of Pt-MG have been previously reported.^{24,28} Briefly, Pt_{57.5}Cu_{14.7}Ni_{5.3}P_{22.5} metallic glass (Pt-MG) was thermoplastically patterned using nanoporous alumina templates. Unpatterned and nanopatterned Pt-MG discs of about 7 mm in diameter and with different surface topologies were fabricated. Nanopatterned samples consisted of vertical nanowires with diameters $d \sim 75$ nm and $d \sim 100$ nm, arranged in a nearly hexagonal lattice with period $p \sim 250$ nm, and attached to a Pt-MG thick (50-150 μ m) substrate. Different lengths of nanowires with $l \sim 500$ nm, $l \sim 1000$ nm and $l \sim 1500$ nm were used in our experiments. A representative SEM image of a patterned Pt-MG sample with $l \sim 1000$ and $d \sim 100$ nm is shown in Fig. 1.1(a).²⁷ The surface topology of the sample was consistent with the template spec due to the high precision of the thermoplastic molding process. Optical images of the same patterned

sample and an unpatterned sample are shown in Fig. 1.1(b) and Fig. 1.1(c), respectively. Evidently, the uniformly dark color of the patterned sample indicates a much lower reflectivity when compared to the unpatterned sample that exhibits a mirror-like metallic surface.

In order to determine the reflectance characteristics of the samples, we measured the integrated diffuse reflectance at different incident angles using three distinct laser sources emitting at $\lambda=532$ nm, 980 nm and 1560 nm using the setup illustrated in Fig. 2.1. In this setup, the scattered light from both the sample and the reference material is collected by an integrating sphere. Under identical conditions, the ratio of the intensity of the scattered light by the sample to the intensity of scattered light by the reference material enables the measurement of integrated diffuse reflectance as a percentage. A calibrated 99% reflectance polytetrafluoroethylene (PTFE) is used in our experiments as the diffuse reference material. We verified the accuracy of the measurements using a 10% Spectralon© diffuse reflectance standard. In detail, a sample holder attached to a computer-controlled rotating stage is used for the angle dependent diffuse reflectance measurements. Data acquisition is automated by a LabView program that is especially developed for this setup. The output intensity of the laser the light is first attenuated by optical density filters and then directed to a beam-splitter. A small fraction of the laser beam was deflected into a detector in order to account for potential laser intensity fluctuations during the measurements. The remainder of the laser beam is then directed to a linear polarizer and a half-wave plate to control the state of polarization of the incident beam before it strikes the sample surface. Finally, a lens was used to focus the laser beam onto the sample which was placed inside the integrating sphere. A second photodetector was placed in one of the output ports of the integrating sphere. The laser reference photodetector (Si photodiode) and the sample photodetector (ILX Lightwave OMH-6703B, Silicon Power Head) were used to monitor the laser light power before and after the laser strikes the surface of the sample, respectively. The contribution from the ambient light is minimized during the data acquisition. The laser beam was carefully aligned, and the beam spot was adjusted such that it probed the center of the sample at all times during the rotation. All the measurements of the samples and the reference material

were carried out at incident angles $-70^\circ < \theta < 70^\circ$ and under the same laser power conditions. The diffuse reflectance of each sample is determined using the formula

$$R = \frac{P_{Sample} - P_{Noise}}{P_{Reference} - P_{Noise}} \times 100 \quad (2.1)$$

where P_{Sample} and $P_{Reference}$ correspond to the intensity of the light reflected by the sample and by the 99% reflectance reference material, respectively. P_{Noise} represents the background intensity measured by the detector attached to the integrated sphere when the laser source is turned off.

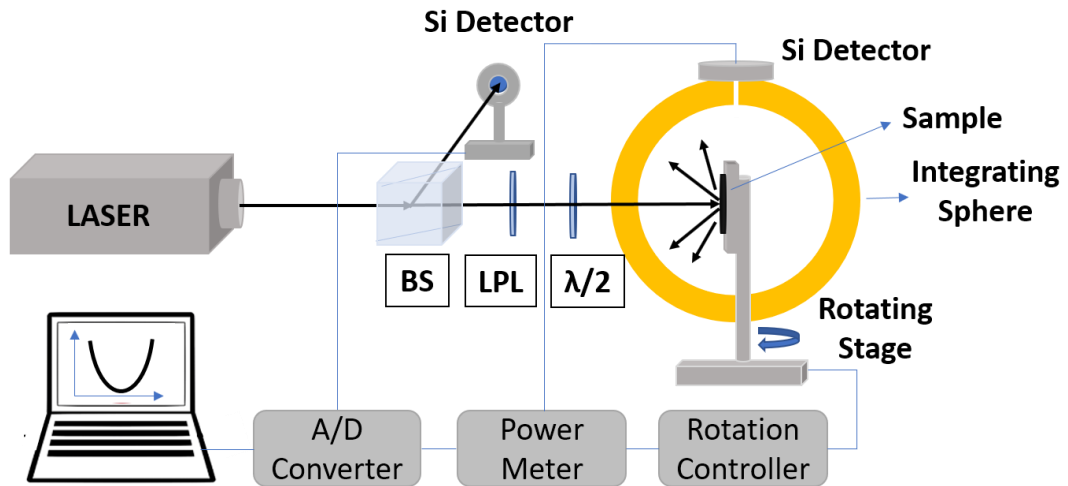


FIG. 2.1 Schematic illustration of the set up used in the integrated diffuse reflectance experiments: BS: beam splitter, LPL: linear polarizer, $\lambda/2$: half-wave plate.

2.3 Results and Discussion

2.3.1 Effects of the Nanowire Aspect Ratio on the Integrated Diffuse Reflectance of MG

In order to determine the influence of the aspect ratio on the diffuse reflectance of patterned MG-NWA in the near infrared region, we measured the integrated diffuse reflectance (R) of several samples at different incident angles (θ_i) at $\lambda = 980$ nm wavelength. Diffuse reflectance measurements of two nanopatterned samples with high

aspect ratio $l/d \sim 10$ (HAR) and low aspect ratio $l/d \sim 5$ (LAR) and a flat (F) sample were compared.

Figure 2.2 shows measured and simulated angular dependence of reflectance for both nanopatterned and flat samples. Reflectance as low as $\sim 5.5\%$ over a wide range of incident angles (for $|\theta_i| < 30^\circ$) was determined for the patterned sample with high aspect-ratio nanowires ($l/d \sim 10$). The reflectance increases to $\sim 15.5\%$ and $\sim 50\%$ for lower aspect-ratio ($l/d \sim 5$) nanowires and flat sample, respectively. Multiple reflections of the incident light from the nanowires lead to multiple absorption events that lower the overall reflection from the sample. As the aspect ratio increases, the surface-to-volume ratio increases as well and this results in enhanced absorption. The observed dip in the reflectance near $\theta_i = 0^\circ$ (specially for flat sample, F) is an experimental artifact that is caused by the specular reflectance from the sample and it is due to the loss of scattered light back to the incident port of the integrating sphere.

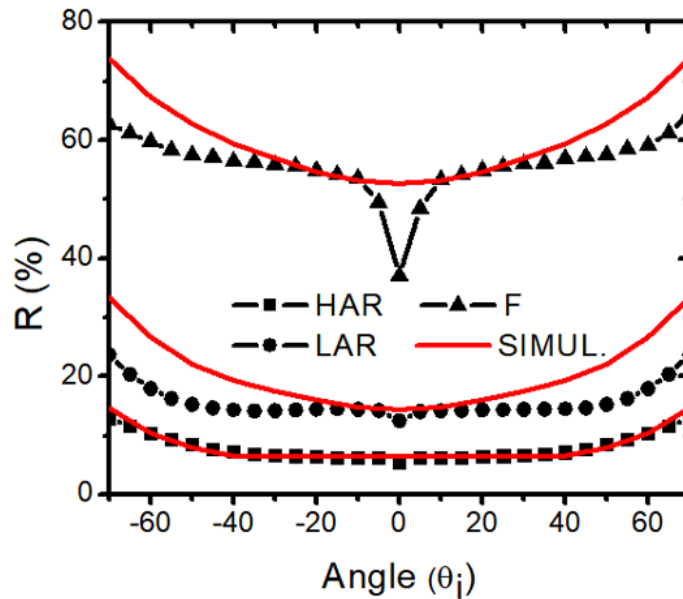


FIG. 2.2 Measured and simulated angular dependence diffuse reflectance of patterned (HAR and LAR) and flat (F) samples at $\lambda=980\text{nm}$.

2.3.2 *Wavelength Dependence of Integrated Diffuse Reflectance*

We investigated the wavelength dependence of the diffuse reflectance of nanopatterned Pt-MG samples both experimentally and with RCWA simulations. Three distinct lasers emitting at wavelengths $\lambda = 532$ nm, 980 nm, and 1560 nm were employed in our diffuse reflectance setup shown in Fig. 2.1. In the case of $\lambda = 1560$ nm, we have used Ge photodiodes as the detector elements.

Figure 2.3 shows the measured and simulated diffuse reflectance of a representative $l/d \sim 10$ aspect ratio sample at incident angle $\theta_i = 10^\circ$ as a function of wavelength of illumination. Reflectance as low as $\sim 1\%$ was determined for our sample at wavelength $\lambda = 532$ nm. The reflectance increases to $\sim 6\%$ and $\sim 20\%$ for $\lambda = 980$ nm and 1560 nm for the same sample, respectively. We measured the diffuse reflectance of nanopatterned samples with other aspect ratios ($l/d \sim 5$ and 15) at these distinct wavelengths and observed similar trends. As the wavelength increases, the nanowire topology appears as a homogeneous media to the infrared light because the spacing between the nanowires is much smaller than the incident wavelength. Similarly, in the visible region, incident wavelength is in the order of porosity of the nanowire surface resulting in higher absorption of the incident light due to multiple reflections between the nanowires. In addition, it is evident from the measured monotonically increasing optical constants of flat Pt-MG samples given in Figure 6.5 that the reflection increases with the wavelength according to the Eq. (2.2).

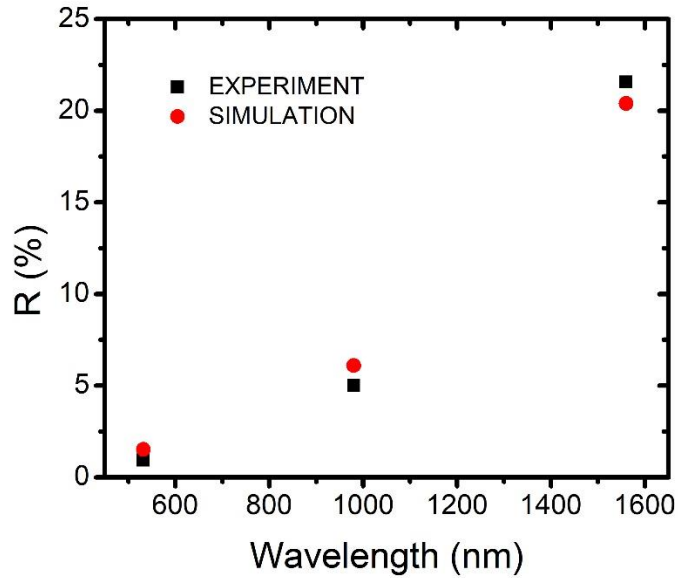


FIG. 2.3 Experimental and simulated diffuse reflectance of Pt-MG nanowires with $l/d \sim 10$ aspect ratio at $\lambda = 532\text{nm}$, 980nm , and 1560nm and incident angle $\theta_i = 10^\circ$.

2.3.3 Rigorous Coupled Wave Analysis Simulations of Diffuse Reflectance

We performed all our diffuse reflectance simulations using a commercial software (DiffractMOD®), that is based on Rigorous Coupled Wave Analysis (RCWA) method. RCWA method is widely employed in problems involving scattering on structures with periodic boundary conditions. In RCWA, the Maxwell's equations are solved using Fourier spatial expansion of the periodic dielectric function in a semi-analytical way. The analyzed structure is assumed to be uniform in the z -direction (direction of incident illumination) and periodic in the lateral (x, y) directions. The structure is sliced into layers along the z -direction where solutions remain analytical while the Fourier expansion of the fields are evaluated in the x - y plane. Combining these Fourier field components with the wavevectors in a matrix whose size is determined by the number of spatial harmonics in the expansion, the propagation of light through each layer is described. Then reflection, transmission, diffraction efficiencies, and field distributions are evaluated by applying appropriate boundary conditions to each layer. Numerical convergence and accuracy of the evaluation is determined by the number of spatial harmonics in the expansion.

DiffRACTMOD® requires an input file of the 3-D layout of the structure which is generated by a Matlab® program specifically developed for generating vertically aligned and bundled nanowire topologies. Figure 2.4 shows a representative layout of a MG structure that consists of 19x19 nanowires with height $h \sim 1000\text{nm}$, diameter $d \sim 100\text{nm}$ and periodicity $p \sim 250\text{nm}$ placed onto a $1\ \mu\text{m}$ thick layer of MG substrate in a triangular lattice arrangement. Variations to these topological parameters (Δh , Δp , and Δd) are introduced throughout the structure randomly to better mimic the sample that contains fluctuations of these parameters (as evident from the SEM image shown in Fig. 1.1 (a)) due to imperfections in the fabrication process. Besides the topological parameters, optical parameters of the material such as wavelength dependent refractive index $n(\lambda)$ and extinction coefficient $k(\lambda)$ are required to evaluate the diffuse reflectance. Figure 6.5 shows the optical constants of flat Pt-MG determined from Spectroscopic Ellipsometry (SE) measurements which will be discussed in detail in Chapter 6.

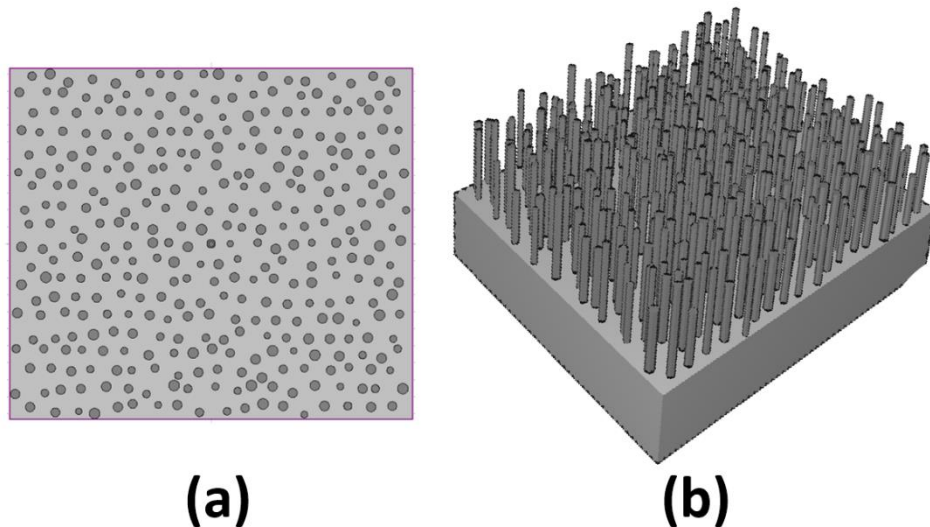


FIG. 2.4 Nanowire design layout of (a) the top view (b) 3D-view for a sample, parameters $l \sim 1000$, $d \sim 100\text{nm}$, and $p \sim 250\text{nm}$ with 50% variation in the NW period, length, and diameter.

We simulated the diffuse reflectance of all investigated flat and nanopatterned samples with different topological parameters and different wavelengths of incident light. Figure

2.2 shows the simulated angle dependence of diffuse reflectance for high aspect ratio (HAR), low aspect ratio (LAR) and flat (F) samples at $\lambda=980\text{nm}$. Differences between simulated and measured diffuse reflectance at higher angles of incidence, especially for the flat and low aspect ratio samples, stem from the contribution of the two polarization states (TM and TE). Although this is the case, the good agreement between the measurement and simulation is evident for incident angles $|\theta_i|<30^\circ$.

The wavelength dependence of simulated and measured diffuse reflectance of a nanopatterned sample ($l/d\sim 10$) at $\theta_i = 10^\circ$ is presented in Fig. 2.3. The simulated results were determined to be within $\sim 0.07\%$ of the actual measurements indicating that RCWA is a useful method that can adequately describe the wavelength dependence of the diffuse reflectance of the MG nanowire arrays.

2.4 Enhancing Reflectance: Bundling Effect of Vertically Aligned Nanowires

Although increasing the aspect ratio (l/d) of nanowires results in higher absorption, nanowires with aspect-ratios exceeding 20 are susceptible to bundling after removal from the template by wet etching due to capillarity forces. Exposing vertically aligned high aspect ratio nanowires to a liquid environment results in undesirable reduction in surface-to-volume ratio and distortion of metallic glass nanowires.²⁸ Here, we show that bundling is not a limiting factor to achieve low reflectance, but it is an effect that can be tuned to further enhance the absorption of the nanowire topology. We studied the reflectance of the bundled metallic glass nanowires using diffuse reflectance measurements and RCWA simulations.

Vertical nanowires with the aspect ratio of $l/d \sim 20$ were prepared by thermoplastic embossing and supercritical CO_2 drying as described in our previous work.²⁸ Vertically aligned nanowires were soaked in DI water and dried in air to induce bundling. The diffuse reflectance of the bundled samples were compared to those obtained from the same samples before bundling in order to confirm that any change in optical response is directly correlated to the profile of the nanowires while all other topological parameters kept the same. Figures 2.5(a) and 2.5(b) show representative SEM images of vertically

aligned and bundled Pt-based metallic glass nanowires with $d \sim 75$ nm and $l \sim 1500$ nm, respectively.

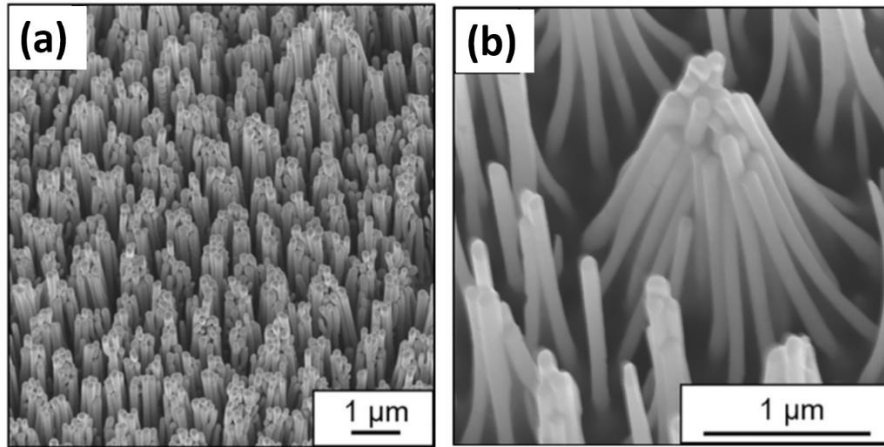


FIG. 2.5 SEM images of a patterned Pt-MG: (a) vertically aligned, and (b) bundled.²⁸

A $\lambda = 1560$ nm infrared laser was employed in the integrated diffuse reflectance experiments using the setup shown in Fig. 2.1. Once again, the accuracy of the measurements were verified using the same 15% (at 1560 nm wavelength) Spectralon® diffuse reflectance standard. The diffuse reflectance of vertical and bundled metallic glass nanowires ($d \sim 75$ nm, $l \sim 1500$ nm) at different incident angles are shown in Fig. 2.6. The bundled sample exhibited lower reflectance when compared to the unbundled one within the same incident angle range. A common sharp dip in the reflectance near 0° angle is an experimental artifact arising from the loss of scattered light back to the incident port aperture of the integrating sphere due to the specular reflection from the sample. In order to verify the experimental results, we simulated the diffuse reflectance of bundled and unbundled samples using the same RCWA solver described above. The optical constants of Pt-based metallic glass required for the simulations will be detailed in Chapter 6. An overall agreement between simulated and measured diffuse reflectance is evident from Fig. 2.6. Our simulations further confirm that the bundling of the nanowires results in the reduction of the reflectance. Similar diffuse reflectance experiments performed on metallic glass nanowires of other diameters ($d \sim 55$ nm and 100 nm) have also revealed a reduction in the infrared diffuse reflectance upon bundling.

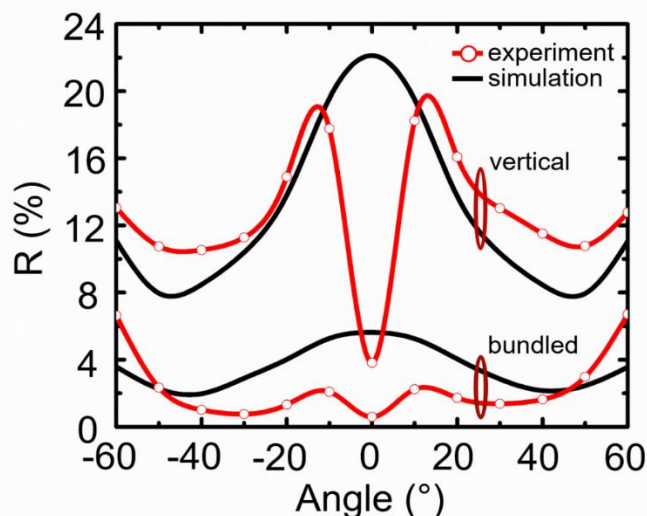


FIG. 2.6 The angular dependence of measured and simulated diffuse reflectance of vertically aligned and bundled samples at $\lambda=1560$ nm.²⁸

The effect of bundling on the reflectance can be understood based on fundamental optics. According to Fresnel's law, the specular reflectance (R) at normal incidence for a material placed in air is given by

$$R = \frac{(1-n)^2 + k^2}{(1+n)^2 + k^2} \quad (2.2)$$

where n and k are the real and imaginary parts of the material refractive index, respectively. Equation (2.2) suggests that the reflectance can be reduced by decreasing the refractive index at the material-air interface. The metallic glass surface with vertical nanowires appears as a homogeneous media to the infrared light because the spacing between the nanowires is much smaller than the incident wavelength. In contrast, bundling results in the formation of air pockets with dimensions comparable to the incident wavelength. This results in gradual change in the effective refractive index at the air-metallic glass interface which lowers the reflectance. Similar findings have been reported in highly absorbing carbon nanotubes and Si nanowire forests.^{9,29,30}

The extent of bundling can be further controlled using solvents with different surface tensions as reported in our previous work.²⁸ Figure 2.7 shows the effect of extent of bundling on diffuse reflectance using RCWA simulations. CAD profile of the simulated

vertically aligned nanowire array and the bundled structures are given in Figs. (b) and (c-e), respectively. In order to illustrate the effect of bundling in the diffuse reflectance of MG nanowires, we performed RCWA simulations using nanowires with average numbers of 4, 8, and 12 in a bundle as shown in Figs. 2.7(c), (d), and (e), respectively. It is evident that over 80% of reduction of diffuse reflectance is achievable by increasing the extent of bundling (number of nanowires in a bundle). This offers a unique opportunity to tailor the properties of nanowires without changing their aspect-ratios.

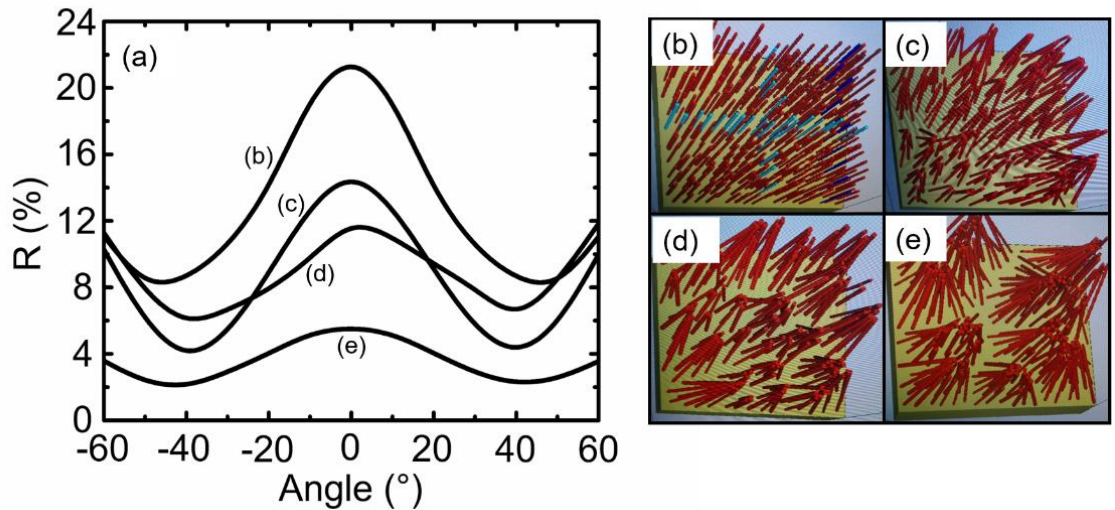


FIG. 2.7 (a) Simulated angular dependence of diffuse reflection at $\lambda = 1560$ nm for Pt-MG nanowires of $d \sim 75$ nm $l \sim 1500$ nm with different bundling profiles. (b) CAD profile of the simulated vertically aligned structure. (c-e) CAD profiles of simulated bundled structures with 4, 8, and 12 average number of nanowires in a bundle.

2.5 Conclusions

We demonstrated the effects of the aspect ratio and the incident wavelength on the diffuse reflectance of nanopatterned Pt-MGs in the visible and near infrared regions. Higher aspect ratio samples exhibited lower reflectance for all the incident angles. The large absorption efficiency is attributed to the reduced effective index of refraction of the nanowire topology in the near infrared region, due to the increased surface to volume ratio. In the visible region, light trapping results in increased absorption.

RCWA simulations were used to verify the diffuse reflectance measurements. A good agreement between experiments and simulations were obtained indicating that RCWA

analysis can be used to optimize the nanowire topology in order to minimize the reflectance of MG-NWRs. We showed that further reduction of the diffuse reflectance can be achieved by tuning the degree of bundling of the Pt-MG nanowires by exposing them to different liquid environments. Our results suggest that Pt-MG nanowires can potentially be utilized in photo-thermal energy conversion applications due to their low reflectance.

CHAPTER 3

SPECKLE IMAGE ANALYSIS OF METALLIC GLASS SCATTERERS VIA CLASSIFIER ALGORITHM

3.1 Introduction

Scattering of light from rough surfaces are known to generate speckle images. These speckle images stem from the random distribution of scalar fields and phases scattered from the material. Although the formation of laser speckles is not desired for many applications, they are important in a wide range of applications such as microscopy,³¹ interferometry,³² material processing,³³ and dynamic imaging in biomedicine³⁴. The statistical analysis of the speckle images enabled the identification of different types of dielectrics and roughness determination of metallic surfaces.^{33,35} Most of the speckle images are realized in the far-field. Therefore, the smaller features on the material surface is likely to be the responsible for the dominant features of the speckle images. Thus, in order to understand the mechanisms underlying the speckle image formation, a detailed knowledge of the surface roughness is critical. The ability to pattern metallic glasses with different structural states (amorphous and crystalline) at the nano and micro scales controllably is very attractive for investigating the correlation between the statistical parameters of the speckle images and the topology and material composition used to generate them. However, speckle image analysis using metallic glass scatterers has not been investigated thus far. Here we investigated the far-field speckle patterns of metallic glass samples comprising arrays of nanowires with different aspect ratios, roughnesses, and structural states. All measured speckle patterns were obtained under identical optical illumination and detection conditions.

Figure 3.1 shows a simplified schematic illustration of the speckle image acquisition and processing analysis. The measured speckle images were split into training and testing sets. The training set represents a group of speckle images that are used to “teach” the algorithm about the different types of samples (also known as classes). The testing set is a collection of speckle images that is used to assess the accuracy of the algorithm to predict the class of any new speckle image inputted into the algorithm. Using a Matlab®

program, we extracted the statistical parameters established in image processing literature for each speckle pattern in the training set.³⁶ The ability of the parameters to distinguish one sample from the other based on the given algorithm is ranked by Attribute Evaluator in Waikato Environment for Knowledge Analysis (Weka).³⁷ We evaluated different machine-learning algorithms such as IBk,³⁸ SMO,³⁹ Naïve Bayes,⁴⁰ and Logistic Regression⁴¹ that best distinguish our samples based on these optimized parameters using Weka. The accuracy of each classifier is initially tested using 10-fold cross validation on the training set. We further demonstrated that all these classifier algorithms can be used to successfully classify any new speckle image in the testing set. Therefore, we show that it is possible to identify the nanowire topology and structural state of patterned metallic glass samples from their speckle images.

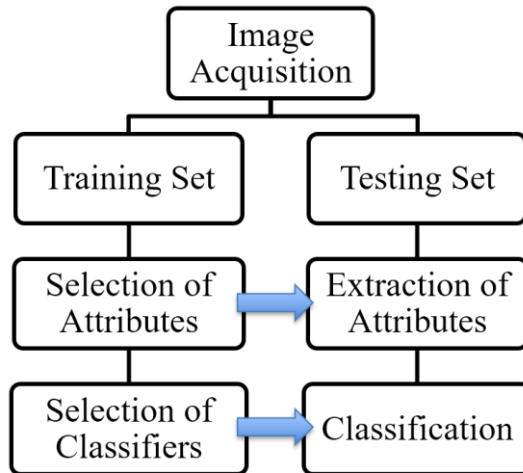


FIG. 3.1 Schematic illustration of the main tasks used to perform the classification of speckle images.

3.2 Experimental Details

Discs of about 8 mm diameter unpatterned samples of different structural states (amorphous and crystalline) and nanopatterned Pt-MG samples with different surface topologies were fabricated as described in the previous chapter. Unpatterned amorphous and crystalline samples of similar roughness ($\sim 0.1\mu\text{m}$) were prepared. Nanopatterned samples consisted of vertical nanowires with diameters $d\sim 50\text{nm}$ and $d\sim 100\text{nm}$, arranged in a nearly hexagonal lattice with period $p\sim 250\text{nm}$, and attached to Pt-MG substrate. Different lengths of nanowires with $l\sim 500\text{nm}$ and $l\sim 1200\text{nm}$ were studied. The

characteristics of the 5 samples ($M=5$ classes) investigated in this study and their respective speckle images are shown in Fig. 3.2. It is evident from Fig. 3.2 that the speckle images exhibit similar scattering characteristics and are not clearly distinguishable from one another.

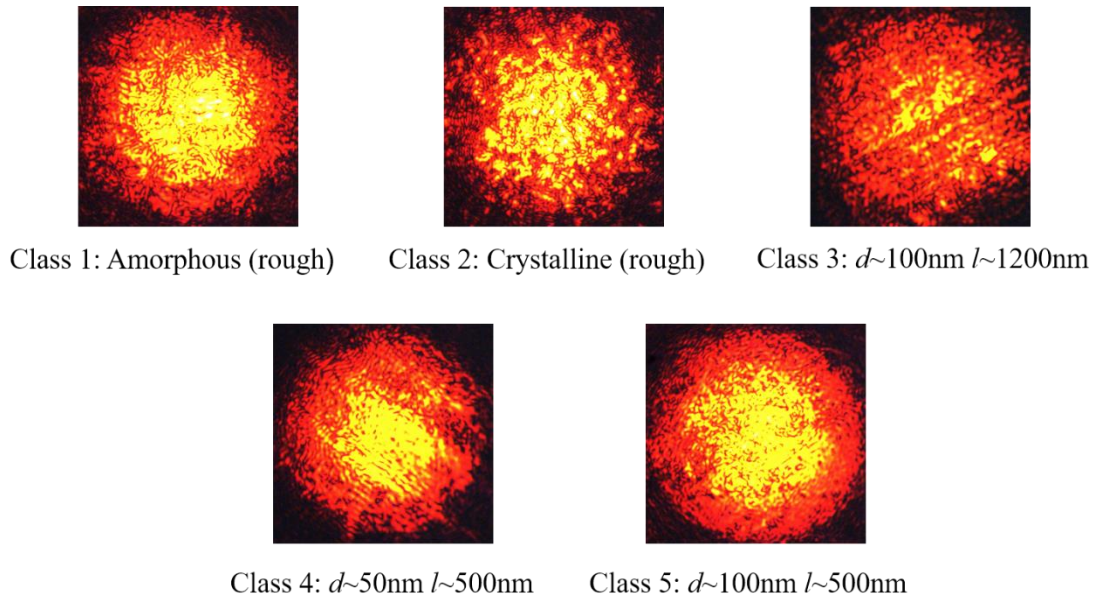


FIG. 3.2 Speckle images of samples with different topologies and structural states corresponding to each class.

The speckle image acquisition was performed using an experimental diffuse micro-reflectance setup which is illustrated schematically in Fig. 3.3 (a). A CW He-Ne laser emitting at $\lambda=633$ nm was used as the illumination light source. All the samples were illuminated at normal incidence under identical magnification provided by a microscopic objective lens (40x). In order to acquire multiple speckle images at different regions of the same sample surface, we have placed the sample over a motorized x-y translation stage. $2N=36$ speckle images were collected for each sample by scanning the sample surface in the x-y plane at increments of $\sim 100\mu\text{m}$ in a 6x6 matrix form. The scattered light from the samples were collected and imaged by a CCD camera. Figure 3.3 (b) shows a representative speckle image collected from the patterned MG sample with aspect ratio $l/d\sim 12$ using the setup shown in Fig. 3.3 (a).

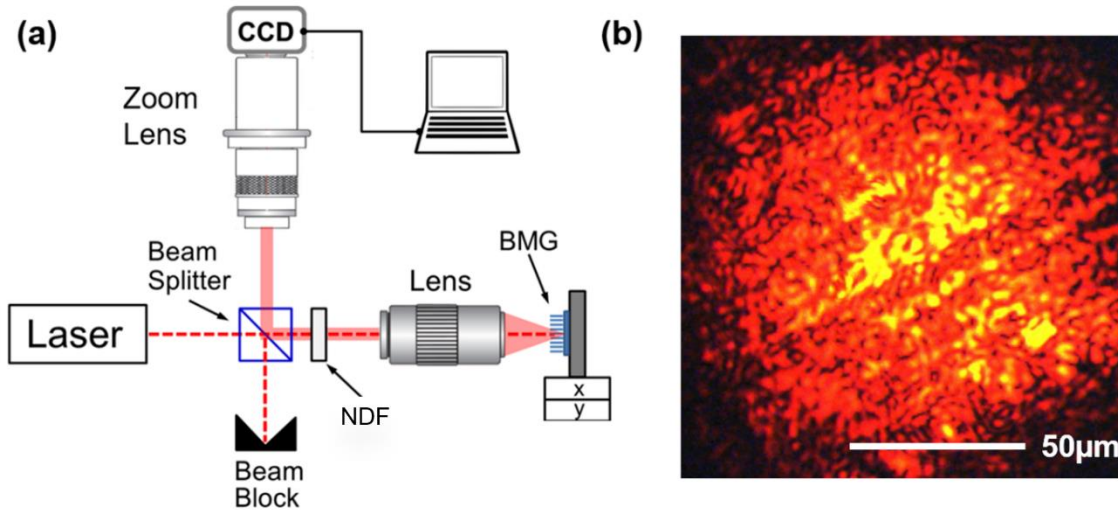


FIG. 3.3 (a) Schematic illustration of the set up used in the speckle image acquisition experiments (b) a representative speckle image of the Pt-MG nanowire sample with aspect ratio $l/d \sim 12$.

3.3 Results and Discussion

3.3.1 Selection of Statistical Parameters

A Matlab[®] code was developed to extract 11 statistical parameters from each speckle image collected from each sample. These well-known parameters include the contrast (C), skewness (S), and several moments of logarithm of power spectral density ($\langle u_R^{-4} \rangle$, $\langle u_R^{-2} \rangle$, $\langle u_R^{-1} \rangle$, $\langle u_R^0 \rangle$, and $\langle u_R^1 \rangle$) and related parameters (C_{max} , C_{width} , C_0 , and V). Details of the origin of these statistical parameters and their significance can be found elsewhere.^{35,36} The speckle images acquired from different regions of each sample were separated into two categories: the training set and the testing set. Each set contains $N=18$ speckle images per sample and a total of $M \times N = 90$ speckle images per set were used in the analysis of each sample. The statistical parameters extracted from the training set of each sample were used as the signature to distinguish between classes. It is critical to find out the parameters that are the most appropriate for classifying our samples to reduce the computational time and to improve accuracy of the algorithm. In order to achieve this, we evaluated the ability of each statistical parameter to differentiate between classes by

applying the Weka's attribution selection process using the 10-fold cross validation on the training set. Table 3.1 shows the average merit values that are based on the correlation of each parameter with the class value and low correlation with each other for different algorithms investigated in this work. The figure of merit for each parameter is ranked and expressed as a number between 0 and 1. Although the highlighted parameter C_{width} listed in Table 3.1 is ranked last for all the classifier algorithms which were investigated in this work, it has proven to increase the prediction rate for most algorithms and therefore it is included in the evaluation process.

Table 3.1: Average figure of merit ranking of the statistical parameters used in the speckle image classification obtained from different algorithms.

Algorithm	C	S	$\langle u_R^{-4} \rangle$	$\langle u_R^{-2} \rangle$	$\langle u_R^{-1} \rangle$	$\langle u_R^0 \rangle$	$\langle u_R^1 \rangle$	C_{max}	C_{width}	C_o	V
SMO	0.382	0.370	0.269	0.255	0.354	0.331	0.325	0.380	0.095	0.377	0.383
	\pm 0.077	\pm 0.055	\pm 0.047	\pm 0.045	\pm 0.051	\pm 0.031	\pm 0.038	\pm 0.027	\pm 0.033	\pm 0.044	\pm 0.041
IBk	0.637	0.640	0.325	0.440	0.613	0.513	0.529	0.404	0.163	0.469	0.673
	\pm 0.028	\pm 0.032	\pm 0.037	\pm 0.037	\pm 0.019	\pm 0.023	\pm 0.026	\pm 0.036	\pm 0.016	\pm 0.027	\pm 0.023
Logistics	0.616	0.685	0.407	0.313	0.564	0.503	0.487	0.497	0.196	0.522	0.696
	\pm 0.016	\pm 0.017	\pm 0.031	\pm 0.018	\pm 0.018	\pm 0.018	\pm 0.027	\pm 0.017	\pm 0.025	\pm 0.024	\pm 0.023
Naïve Bayes	0.633	0.678	0.432	0.406	0.688	0.628	0.637	0.498	0.180	0.535	0.701
	\pm 0.017	\pm 0.010	\pm 0.022	\pm 0.021	\pm 0.015	\pm 0.019	\pm 0.010	\pm 0.018	\pm 0.036	\pm 0.031	\pm 0.014

3.3.2 Selection of Classifier Algorithms

After optimizing the statistical parameters, we ranked the algorithms based on their performances using the Weka Experiment Environment³⁷ in order to determine the classifier with the most predictive accuracy. The evaluated multi-class functions include lazy IBk, Naïve Bayes, Logistic Regression, and SMO.³⁸⁻⁴¹ The IBk algorithm, also known as k-nearest neighbor, is based on the evaluation of the distance between the k-close instances in the known data (training) and applying these instances to the unknown

(testing) data. In Naïve Bayes, the prior probability of each class is calculated based on the training data and applied to predict the class with the highest probability. Logistic Regression assigns a coefficient for each parameter in the training set, linearly combines them into a regression function, and transforms them using a logistic function. The SMO algorithm, also known as SVM (Support Vector Machines), finds the straight line that best distinguishes different classes and it only evaluates the instances in the training set based on how close they are to that line that separates classes from each other. Figure 3.4 shows the accuracies of these classifiers based on 10-fold cross validation on the training data. Evidently, the IBk algorithm has the highest accuracy of 100% and is the most suitable for our data set. However, the high accuracies of 99.67% for SMO, 99.22% of Logistic Regression, and 98.89% Naïve Bayes suggest that they can also be used efficiently if desired.

Dataset	(1) lazy.IBk	(2) bayes	(3) funct	(4) funct	
SPR	(100)	100.00	98.89	99.22	99.67
	(v/ /*)	(0/1/0)	(0/1/0)	(0/1/0)	

Key:
 (1) lazy.IBk '-K 1 -W 0 -A \"weka.core.neighboursearch.LinearNNSearch -A
 (2) bayes.NaiveBayes '' 5995231201785697655
 (3) functions.Logistic '-R 1.0E-8 -M -1 -num-decimal-places 4' 393211703
 (4) functions.SMO '-C 1.0 -L 0.001 -P 1.0E-12 -N 0 -V -1 -W 1 -K \"funct:

FIG. 3.4 Performance evaluation of multi-class functions in Weka using 10-fold cross validation on the training data.

3.3.3 Identifying a Sample Using Speckle Images

After optimizing the statistical parameters and the classifier algorithms, we tested the ability of each algorithm to predict and classify new instances provided by the testing set. In order to accomplish this task, we used $N=90$ number of speckle images in the testing set as input and run the algorithm to classify each speckle image based on learned $M=5$ classes corresponding to 5 samples. A schematic representation of this classifier flow process and the rate of correctly classified instances based on the testing set are presented in Figs. 3.5 (a) and (b), respectively. SMO, IBk, and Logistic Regression algorithms can

identify the given sample based on its speckle images with 100% accuracy and the Naïve Bayes classified 1 out of 90 instances incorrectly.

The ability to distinguish very similar samples from each other based on the parameters derived from their speckle images demonstrate that there are subtle differences between the speckle images generated by each type of sample. Although the parameters $\langle u_R^{-2} \rangle$, $\langle u_R^{-1} \rangle$, $\langle u_R^0 \rangle$, and $\langle u_R^1 \rangle$ that are derived from the logarithm of power spectral density are proven to be very useful in the classification of all the samples investigated in this work, the contrast (C) was a very important parameter for distinguishing the high aspect ratio samples (Class 3 in Fig. 3.2) from the lower aspect ratio samples (Class 5 in Fig. 3.2). This is mainly due to the higher aspect ratio sample with higher absorption emitting less scattered light and thus, resulting in speckle images with higher contrast. A comparison between the amorphous and crystalline samples with similar roughness indicates the importance of the parameter V , corresponding to the variance of power spectral density in logarithmic scale. Although we can identify an amorphous sample from a crystalline sample with 100% accuracy for most algorithms, further investigation is required to apprehend the physical relationship between the structural state of the material and their speckle images.

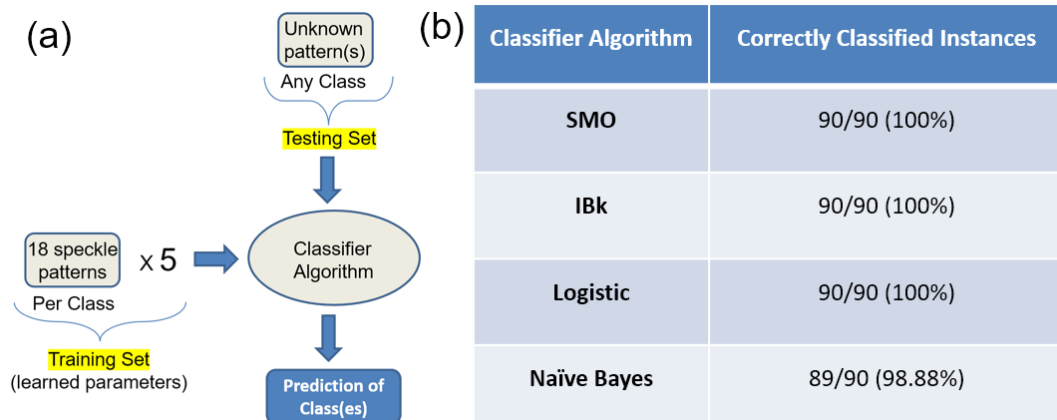


FIG. 3.5 (a) Classifier flowchart (b) rate of instances correctly classified by SMO, IBk, Logistic, and Naïve Bayes classifier algorithms, respectively.

3.4 Conclusion

Using far-field speckle image analysis, we demonstrated that it is possible to identify metallic glasses with different aspect ratios, amorphicity, and crystallinity with ~100% accuracy using machine learning algorithms. We demonstrated the selection process of the statistical parameters and the implementation of the selected parameters into various classifier algorithms that are used to distinguish our samples from each other. The ability to distinguish the high aspect ratio samples from the low aspect ratio ones, in their amorphous states suggests that speckle image analysis can be used to evaluate the absorption properties of the sample based on its surface characteristics. Similarly, we showed that speckle images from amorphous and crystalline samples with similar surfaces can be distinguished from each other. This suggests that specific composition information regarding the volumetric scattering could also potentially be extracted from statistical analysis of the speckle images.

Although it is evident that the speckle pattern of a sample carries the information regarding the surface and material composition and it is sufficient to recognize a sample from a set of other similar samples, further investigation is required to understand the relationship between the speckle images and their corresponding surface roughness characteristics. This can be potentially achieved by introducing polarization and angle dependent analysis of the speckle images and realizing more accurate statistical parameters corresponding to the physical properties of the investigated materials. This will be explored in the near future.

CHAPTER 4

PHOTO-INDUCED HEAT LOCALIZATION OF NANOSTRUCTURED METALLIC GLASSES

4.1 Introduction

We have previously demonstrated that low reflectance over a wide range of incident angles and frequencies can be achieved with arrays of MG nanowires of different topological characteristics. The ability to pattern MGs at different length scales (from nanometer to centimeter) is very attractive to realize surface structures with high absorption and heat transport characteristics for photo-thermal energy conversion applications. However, the correlation between the absorption properties and the photo-induced heating of MG nanowires has not been explored thus far.

In this chapter, we report photo-thermal studies on low reflectance Pt-MG samples patterned with arrays of nanowires using a near-infrared laser as the illumination source. Thermography measurements revealed marked photo-induced spatial heat localization and high temperature rise at moderate laser excitation powers. This attribute enables the use of nanostructured MGs for photo-thermal energy conversion and the generation of programmable arbitrary patterns for mid-IR image applications.

4.2 Experimental Details

In these experiments, Pt-MG discs of 9 mm diameter were prepared by thermoplastic embossing against nanoporous alumina templates (under 100–300MPa) as described in Chapter 2. Pt-MG samples investigated here consist of arrays of vertical nanowires with average diameter $d=100\text{nm}$, length $l=2000\text{nm}$, and period $p=254\text{nm}$. A representative SEM image of a patterned Pt-MG sample investigated here is shown in Fig. 4.1(a). The wire diameters were close to the template spec indicating the high fidelity of the thermoplastic molding process. An optical image of the same sample is shown in Fig. 4.1(b). Similarly to Fig. 1.1, the uniform dark color of the sample over the entire patterned area revealed both very low reflectivity and high uniformity of the texturing process. For comparison purposes, we also investigated a commercial black anodized

aluminum (BAA) sheet whose SEM and optical images are shown in Figs. 4.1(c) and 4.1(d), respectively. Similar to the Pt-MG, the BAA sample exhibited very low reflectance [Fig. 4.1(d)], but its random granular microscopic topology [Fig. 4.1(c)] is markedly different from that of the Pt-MG sample [Fig. 4.1(a)].

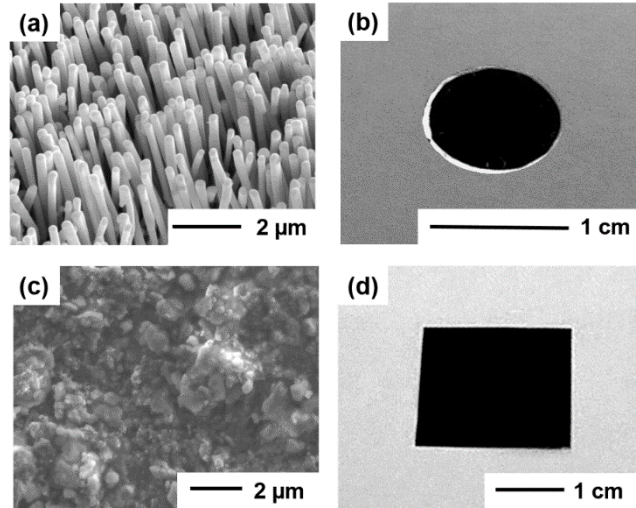


FIG. 4.1 (a) and (c) SEM images and (b) and (d) optical images of the patterned Pt-MG and BAA samples, respectively.⁴²

In order to determine the absorption (A) characteristics of the samples shown in Fig. 4.1, we measured the integrated diffuse reflectance (R) at different incident angles at $\lambda=980$ nm using the procedure described in Chapter 2. Figure 4.2 shows the angular dependent absorption ($A=1-R$) of both samples. Absorption as high as 98.6% and 95.9% over a wide range of incident angles (for $|\theta_i| < 45^\circ$) was determined for the Pt-MG and BAA samples, respectively. The results shown in Fig. 4.2 suggest that the absorption of both samples is very similar, supporting the observed low reflectivity under white light illumination [see Figs. 4.1(b) and 4.1(d)]. The low reflectance shown in Fig. 4.2 is attributed to efficient light trapping and the absorption mechanism due to multiple reflections by the MG nanowires and the nanotextured topology of the BAA sample.

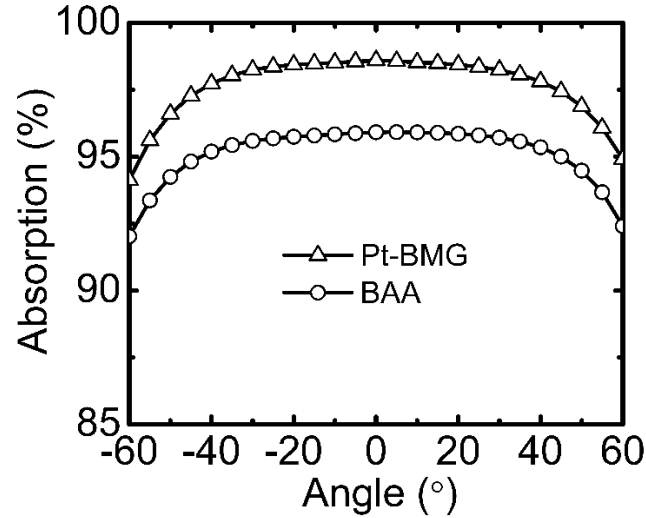


FIG. 4.2 Measured angular dependence of absorption for patterned Pt-MG and BAA samples at $\lambda=980\text{nm}$.⁴²

The photo-induced temperature profiles of the surface of the patterned Pt-MG and BAA samples were determined using the infrared (IR) thermography schematic setup shown in Fig. 4.3 which consists of a continuous wave $\lambda=980\text{ nm}$ semiconductor laser diode, collimating and focusing lenses, dual-axis scanning galvo mirrors, waveform generators to dynamically and independently control the frequencies and vibrating amplitudes of the scanning mirrors, and a 480 x 640 pixel resolution thermal camera. The samples were placed over a solid aluminum block holder and illuminated by the laser with a beam spot size of $250 \times 350\ \mu\text{m}^2$ (when the mirrors were kept in the static position). All the measurements were carried out in air and at room temperature. The thermal profiles were obtained for laser power densities (P) varying from 0.5 to $3.5\text{W}/\text{mm}^2$, and the data acquisition started only after the thermal equilibrium was reached on the sample surface ($\sim 15\text{s}$). Lissajous-like photoinduced thermal patterns were generated on the Pt-MG samples by applying sinusoidal waveforms with different voltage amplitudes and frequencies to each galvo mirror. Real-time thermal images were obtained using the camera's acquisition software.

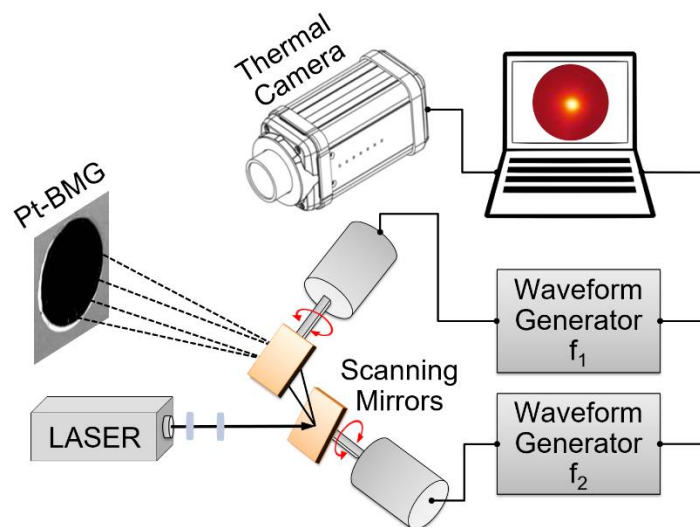


FIG. 4.3 Schematic illustration of the set up used in the photo-thermal experiments.⁴²

4.3 Results and Discussion

4.3.1 Heat Localization Effect

The thermal images of both Pt-MG and the BAA samples under identical laser illumination conditions ($P=1\text{W}/\text{mm}^2$) are shown in Figs. 4.4(a) and 4.4(b), respectively. The thermal images revealed nearly circular hot spot regions at the illuminated areas despite the laser elliptical shape. This is attributed to the larger lateral heat diffusion area when compared to the laser spot size. Although both samples exhibited similar absorption at $\lambda=980\text{ nm}$ (see Fig. 4.2) the photo-induced temperature profiles and maximum temperatures reached are noticeably different. Well-defined spatial heat localization at the laser illuminated area was observed for the Pt-MG sample, where a maximum temperature of 71°C was determined at the center of the hot spot region. In contrast, the maximum temperature on the BAA sample was 26°C which is only slightly above the room temperature, and no evident spatial heat localization was observed in this case [Fig. 4.4(b)]. The corresponding full width at half maxima (FWHMs) obtained from the horizontal temperature line profiles along the photo-induced hot spots were determined as $\sim 1.1\text{mm}$ and $\sim 1.3\text{mm}$ [see Fig. 4.4(c)], respectively, for the Pt-MG and BAA samples. In both cases, the widths of the hot spots on the surface of the samples were larger than the incident laser beam indicating a lateral heat diffusion. The relative temperature contrast

(ΔT) between hot and cold regions observed in the thermal images shown in Figs. 4.4(a) and 4.4(b) can be estimated as $\Delta T = (T_{\max} - T_{\min}) / (T_{\max} + T_{\min})$. We determined $\Delta T = 52.2\%$ and 5.4% for the Pt-MG and BAA samples, respectively, supporting the observed large difference in temperature rise between the two samples under identical laser excitation conditions.

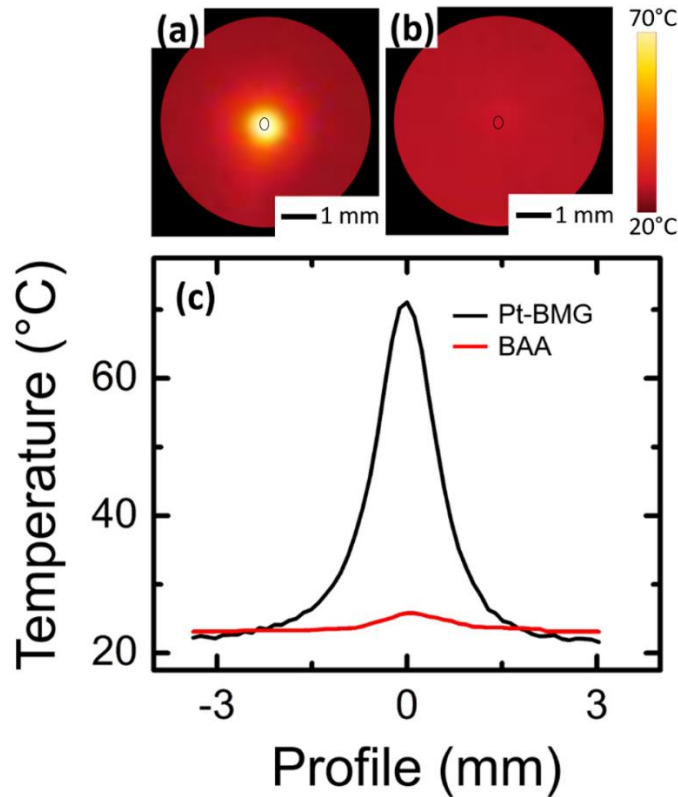


FIG. 4.4 Thermal images of (a) patterned Pt-MG and (b) BAA samples at $P=1 \text{ W/mm}^2$. (c) Horizontal temperature line profiles of the thermal images shown in (a) and (b). The laser spot size (black ellipse) is also illustrated in (a) and (b).⁴²

4.3.2 Excitation Power Dependence of Induced Temperature

In order to further explore the heat localization effects and the temperature rise on the Pt-MG samples, we performed thermographic image analysis at different laser power densities. The corresponding horizontal line profiles along the photo-induced hot spot regions for different laser power densities are shown in Fig. 4.5. The maximum temperature (see the inset of Fig. 4.5) varied from 49°C to 148°C when the power density was increased from 0.5 to 3.5 W/mm^2 , respectively. We determined a FWHM of $\sim 1.12 \pm$

0.03mm from Fig. 3.5 which indicates no further significant increase in lateral heat diffusion as the laser power density is increased.

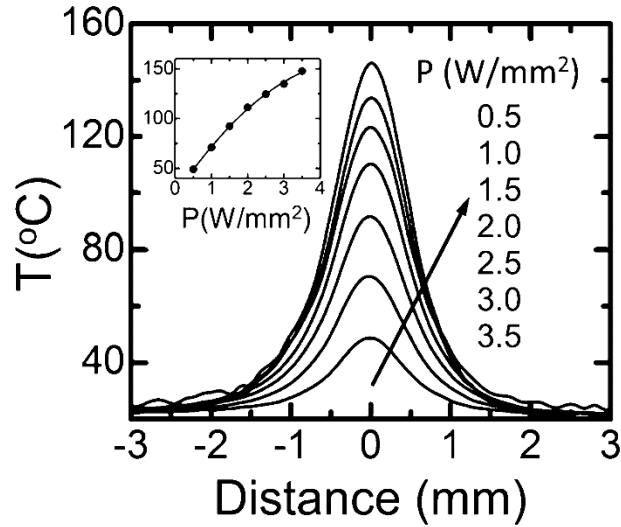


FIG. 4.5 Horizontal temperature line profiles for a patterned Pt-MG sample at different laser power densities. The inset shows the maximum temperature for each laser excitation power density.⁴²

4.4 An Application of Heat Conversion: Infrared Steganography, Tagging, and Tracking

A prospective application of thermography involves steganography where permanent or erasable information is “hidden” on the surface of an object and undetectable to the human eye or conventional CCD cameras, but otherwise visible by a thermal camera. This can be only accomplished, in practice, by generating localized spatial heat at the object’s surface in order to produce well-defined features. As shown in Fig. 4.4(a) the photo-induced heat localization by a laser spot on the surface of patterned Pt-MG samples can be potentially used for steganographic applications. As a proof of concept, we generated Lissajous-like figures on the surface of a Pt-MG sample using the setup shown in Fig. 4.3. In this case, the amplitude, frequency, and relative phase of the waveforms applied to the galvo mirrors were varied to produce the desired patterns. Figure 4.6 shows four examples of photo-induced Lissajous thermal profiles generated on the surface of the same Pt-MG sample. These profiles were obtained by applying sinusoidal waves to both mirrors following the well-known parametric relations defined

as $X(t) = A_1 \cos(2p f_1 t + \phi_1)$ and $Y(t) = A_2 \cos(2p f_2 t + \phi_2)$ where A_1 and A_2 are the amplitudes, f_1 and f_2 are the temporal frequencies, and ϕ_1 and ϕ_2 are the phase angles of the waveforms. The profiles shown in Fig. 4.6 were obtained for different mirror vibration amplitudes, $f_1 = m \times f$ and $f_2 = n \times f$, where m and n are integers (≥ 1) and $f = 50$ Hz, and different relative angular phase shift (ε) between the two waveforms ($\varepsilon = \phi_1 - \phi_2$). The higher temperatures observed at the edges of the Lissajous-like figures are an artifact of the measurements associated with the dynamic response of the galvo mirrors. The well-defined photo-induced images observed in Fig. 4.6 demonstrate the potential of using Pt-MG for steganographic applications. The advantages of the proposed approach for steganography applications include the need of moderate illumination powers while maintaining a well defined temperature contrast between illuminated and non-illuminated areas, the marked photo-induced heat localization, and the fabrication of nanopatterned MGs which can be easily realized via thermoplastic embossing with different topological characteristics.

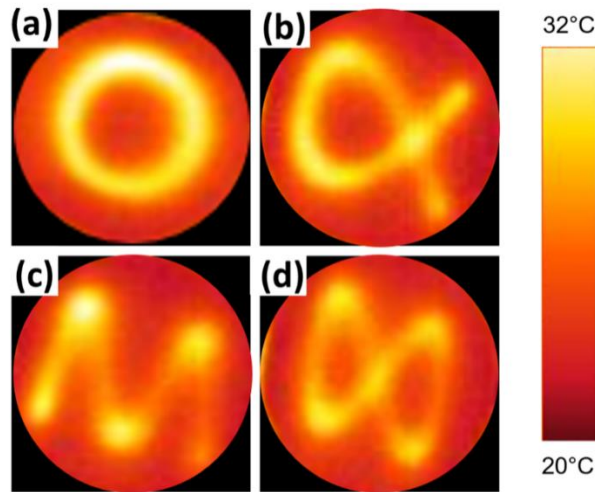


FIG. 4.6 Thermal images of the several Lissajous patterns configured onto patterned Pt-MG. $A_1 = A_2 = 0.2$ V (a) $m = n = 1$, $\varepsilon = \pi/2$, $P = 2.3$ W/mm²; (b) $m = 2$ $n = 3$, $\varepsilon = \pi/4$, $P = 2.5$ W/mm²; (c) $m = 1$ $n = 4$, $\varepsilon = 3\pi/8$, $P = 2.3$ W/mm² (d) $m = 1$ $n = 2$, $\varepsilon = 0$, $P = 2.2$ W/mm².⁴²

Despite the promising results, the larger lateral heat spreading when compared to the illuminated area must be further reduced to realize thermal images with higher spatial

resolution. This can be prospectively achieved by controlling the topology of the nanowires to minimize the presence of additional thermal pathways.

4.5 Conclusions

We demonstrated distinct heat localization and significant temperature rise on low reflectance nanopatterned Pt-MGs illuminated by an infrared laser source. The large photo-thermo energy conversion efficiency was attributed to the reduced thermal conductivity of the metallic nanowires, when compared to the bulk counterpart, due to the increased boundary scattering. The photo-induced localized heat was used to generate programmable thermal patterns on the surface of the investigated samples. Our results suggest that the heat produced by illuminating Pt-MG nanowires can be prospectively used in combination with commercial thermo-electrical generators for photo-thermal-electric energy conversion applications, as broad-band absorbers, and for mid-IR ciphering, steganography, tagging and tracking. We anticipate that further optimization of heat generation can be achieved by tuning the topological parameters of the Pt-MG nanowire samples such as the wire diameter, the periodicity and the length.

CHAPTER 5

PHOTO-INDUCED HEAT CONVERSION ENHANCEMENT OF METALLIC GLASS NANOWIRE ARRAYS

5.1 Introduction

In the previous chapter, we demonstrated a large photo-thermal heating response and strong heat localization effects using MG-NWAs at moderate laser excitation powers. However, quantitative correlation between the MG-NWA dimensions and photo-induced heating has not been established. In particular, theoretical analysis based on coupling of absorption, thermal conversion, and heat transport phenomena is required to understand the photo-thermal behavior of MG nanostructures. To achieve this, we combine simulations and direct temperature measurements in this chapter.

We investigate the effects of MG nanowire characteristics such as, the diameter, the length, and the effect of thickness of the underlying substrate on the photo-thermal response in near-infrared (NIR) region. Infrared (IR) thermography measurements revealed the significance of the substrate thickness and the nanowire aspect-ratio in achieving high temperature during optical illumination. Temperature values measured using thermography of the photo-excited MG nanowires were verified by finite element simulations using COMSOL[®] Multiphysics software. Furthermore, we show that it is possible to induce a phase transformation in MG nanowires from amorphous to crystalline state and yet preserve their geometry. This allows the use of MG nanowires above the glass transition temperature as demonstrated by ignition of thermite powder comprised of aluminum (Al) and copper oxide (CuO) above 500°C using Pt-based MG with a glass transition temperature of 230°C.

5.2 Experimental Details

Once again, we used Pt-MG whose preparation procedure was detailed in the previous chapters. Unpatterned and nanopatterned Pt-MG discs of about 8 mm diameter and different thicknesses were fabricated. All nanopatterned samples consisted of vertical nanowires with diameter $d \sim 100$ nm, arranged in a nearly hexagonal lattice with period

$p \sim 250$ nm, and attached to Pt-MG substrate. Nanowires of other diameters were also studied but for the purpose of theoretical analysis we focus only on 100 nm diameter NWs. The length (l) of nanowires and the thickness (t) of supporting substrate were independently varied to study their effects on photo-induced heating. For convenience, a sample labeling scheme (Table 5.1) is used based on the surface pattern (nanowires) and the substrate thickness. In order to demonstrate the effects of topography and substrate thickness on the photoinduced temperature rise, the samples with nanowires of varying aspect-ratios and two substrate thicknesses (see Table 5.1) were investigated.

Table 5.1: Labeling scheme and description of Pt-MG samples used in this study.⁴³

Label	Nanowire aspect-ratio, l/d	Substrate thickness t , (μm)	Description
F- t_1	-	50	Flat-thin
LAR- t_1	5	50	Low aspect ratio nanowires-thin
HAR- t_1	10	50	High aspect ratio nanowires-thin
F- t_2	-	100	Flat-thick
LAR- t_2	5	100	Low aspect ratio nanowires-thick
HAR- t_2	10	100	High aspect ratio nanowires-thick
VHR- t	>15	100	Very high aspect ratio nanowires

Figure 5.1 shows the schematic and two representative scanning electron microscopy (SEM) images of samples with low and high aspect-ratio nanowires. There is ± 20 nm variation in diameter of nanowires due to pore size distribution in alumina templates. In addition to the amorphous control samples F- t_1 , LAR- t_1 , HAR- t_1 , F- t_2 , LAR- t_2 and HAR- t_2 , two Pt-MG discs with very long nanowires ($l/d > 15$) in amorphous and crystalline states (VHR- t) were prepared to analyze the effect of photo-induced heating on the phase transformation (crystallization, melting, and ignition).

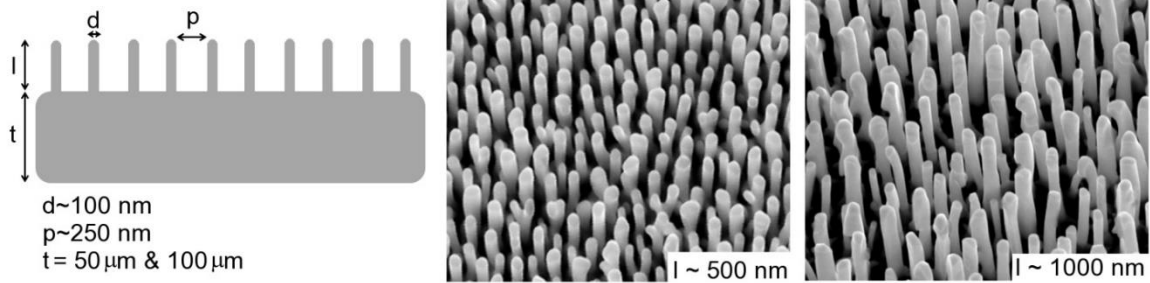


FIG. 5.1 Schematic illustration of sample geometry (not to scale) and SEM images of two Pt-MG samples patterned with nanowires of different lengths.⁴³

5.3 Results and Discussion

5.3.1 Effects of Base Thickness and Aspect Ratio of Nanowires on Absorption

The photo-induced temperature rise on nanopatterned and flat MG surfaces strongly depends on the absorption (A), heat localization, and thermal conductivity of nanowires and the substrate. In order to determine the absorption characteristics of patterned MGs, we measured their integrated diffuse reflectance (R) at different incident angles (θ_i) at $\lambda = 980$ nm using the procedures described in Chapter 2. In short, samples were mounted over a holder that was attached to a computer-controlled rotation stage at the center of an integrating sphere. Samples were illuminated by a continuous-wave laser emitting at $\lambda = 980$ nm and the intensity of the scattered light was measured by a calibrated photodetector that was placed in one of the ports of the integrating sphere.

Figure 5.2 shows measured angular dependence of absorption ($A = 1 - R$) for both nanopatterned (HAR- t_1 , LAR- t_1 , HAR- t_2 , and LAR- t_2) and flat (F- t_1 and F- t_2) samples. Absorption as high as $\sim 94.5\%$ over a wide range of incident angles (for $|\theta_i| < 30^\circ$) was determined for patterned samples with high aspect-ratio nanowires ($l/d \sim 10$). The absorption decreases to $\sim 84.5\%$ and $\sim 50\%$ for lower aspect-ratio ($l/d \sim 5$) nanowire and flat samples, respectively. The large absorption observed for high aspect-ratio nanowires is attributed to the efficient light trapping mechanism due to multiple reflections of incident light. As expected, changes in the substrate thickness do not play any significant role in the optical absorption of the investigated samples. The observed peaks in the absorption near $\theta_i = 0^\circ$ (specially for samples F- t_1 and F- t_2) are experimental artifacts

arising from the loss of scattered light back to the incident port aperture of the integrating sphere as a result of the specular reflection from the samples.

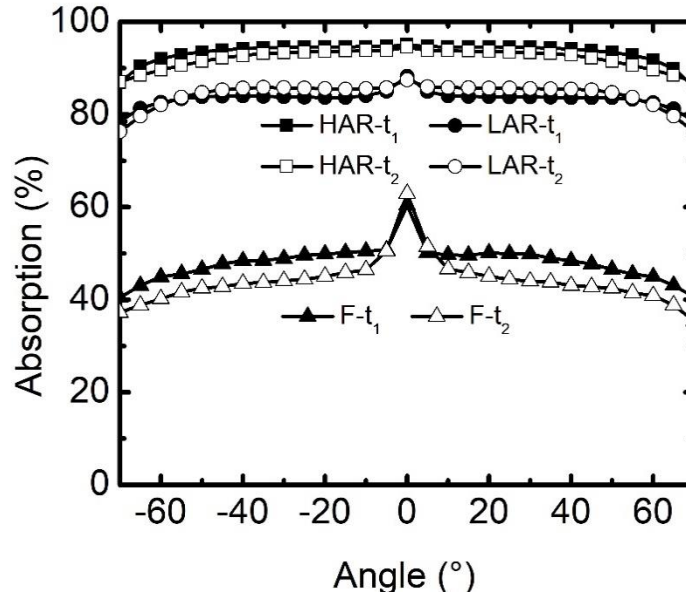


FIG. 5.2 Measured absorption angular dependence of patterned (HAR- t_1 , LAR- t_1 , HAR- t_2 , and LAR- t_2) and flat (F- t_1 and F- t_2) Pt-MG samples at $\lambda = 980$ nm.⁴³

5.3.2 Effects of Base Thickness and Aspect Ratio of Nanowires on Photo-induced Temperatures

The photo-induced temperature rise on the surface of patterned and flat MG samples was determined using the IR thermography setup shown in Fig. 4.3. The edges of MG sample were attached to two glass strips (~ 250 μm thick) forming a rectangular channel on solid aluminum block holder. As a result, both the top and the bottom of the MG samples were exposed to air during the measurements, minimizing the heat loss due to the aluminum holder. The samples were illuminated by a laser with ~ 350 μm diameter spot-size. The maximum temperatures of the illuminated areas were determined for laser power densities varying from 0.5 to 11.5 W/mm^2 using the thermal camera. All data acquisitions were performed at ~ 30 seconds after thermal equilibrium was reached on the sample surface. In this section, we focus on temperature rise up to the glass transition

temperature (T_g) of Pt-MG ($\sim 230^\circ\text{C}$)^{25,44} to avoid potential changes in shape and structural state due to crystallization.

Representative thermal images of a nanopatterned (HAR- t_1) and a flat (F- t_1) Pt-MG sample of same thickness obtained at incident laser power density $\sim 2.8\text{ W/mm}^2$ are shown in Figs. 5.3(a) and 5.3(b), respectively. Strong heat localization at the illuminated area with a maximum temperature rise of about 185°C was determined for the nanopatterned sample (Fig. 5.3(a)). The heat localization is due to significantly lower heat flow in lateral direction in nanowires due to boundary scattering.⁴⁵ In contrast, a diffuse hot spot is observed for the flat sample (Fig. 5.3(b)) and the maximum temperature rise from the room temperature was merely $\Delta T \sim 90^\circ\text{C}$. Lower temperature rise on the flat sample is a combined effect of less optical absorption and higher lateral heat loss in the substrate.

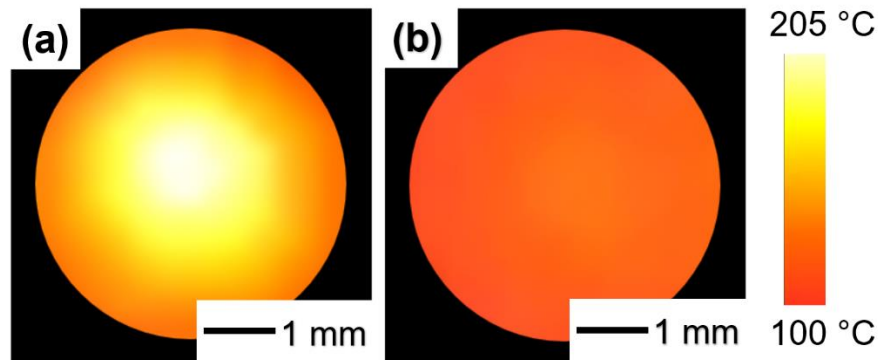


FIG. 5.3 Thermal images of (a) HAR- t_1 and (b) F- t_1 Pt-MG samples obtained at identical laser power density of $\sim 2.8\text{ W/mm}^2$.⁴³

Figure 5.4 shows the maximum temperature values achieved for nanopatterned (HAR- t_1 , LAR- t_1 , HAR- t_2 , and LAR- t_2) and flat (F- t_1 and F- t_2) MG samples illuminated at increasing laser power densities. Photo-induced temperature rise measurements revealed a strong thickness dependence in flat and patterned MGs. For flat samples, the maximum temperatures were measured as $\sim 138^\circ\text{C}$ and $\sim 197^\circ\text{C}$ for thicknesses of $100\ \mu\text{m}$ and $50\ \mu\text{m}$, respectively (at 6.2 W/mm^2). This is attributed to changes in the thermal resistance

with the substrate thickness. Longer conduction path in the thicker substrate results in higher heat loss, and therefore, lower equilibrium temperature. Similar but less pronounced effect of substrate thickness is observed in the nanopatterned samples (Fig. 5.4). This is because the heat transport in the nanopatterned samples is predominantly governed by the conduction through nanowires. Although the samples with similar aspect-ratio nanowires exhibit comparable absorption (see Fig. 5.2), the thinner specimens heat up to higher temperatures (Fig. 5.4). About 52% increase in temperature at 2.8 W/mm^2 was measured when the substrate thickness was decreased by half for high aspect-ratio (~ 10) nanowires. A similar trend was observed for the low aspect-ratio nanowires but with only 31% increase in temperature for the thinner substrate. The difference in maximum temperature in thin and thick samples grows with increasing incident laser power density (Fig. 5.4). Heat conversion is the limiting factor at low laser power density whereas the thermal losses control the temperature at high laser power density.

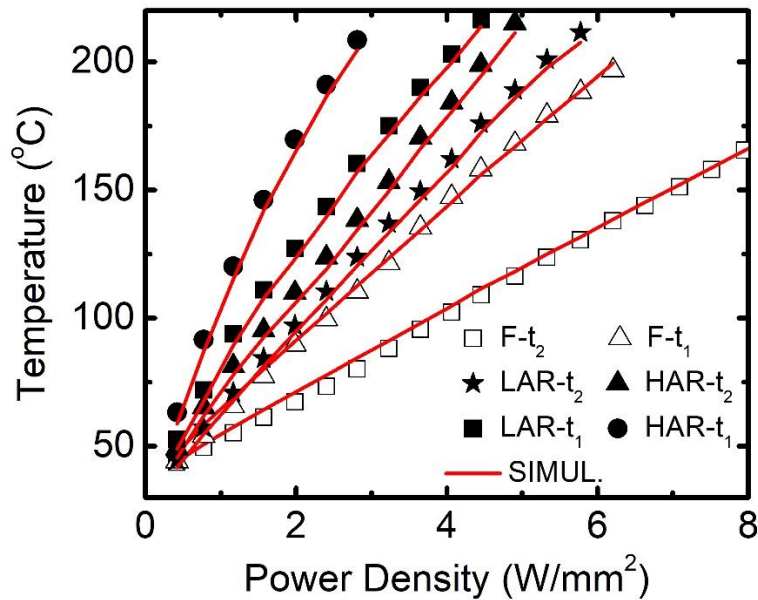


FIG. 5.4 Measured and simulated maximum photo-induced temperature rise for patterned (HAR-t₁, LAR-t₁, HAR-t₂, and LAR-t₂) and unpatterned (F-t₁ and F-t₂) Pt-MG samples at different laser excitation power densities.⁴³

Thermal measurements on the MG samples with similar thickness revealed the importance of surface texture in achieving high photo-induced heat generation. The nanopatterned samples of any thickness generate significantly higher temperatures than the flat counterparts. At an incident laser flux of 4.9 W/mm^2 , the thick patterned samples reach 60% and 82% higher temperatures with nanowires of aspect-ratios of 5 (LAR-t₂) and 10 (HAR-t₂), respectively. Similarly, about 40% (86%) increase in photo-induced temperature was observed with nanowires in thin samples LAR-t₁ (HAR-t₁) at 2.8 W/mm^2 . As shown in Fig. 5.4, due to combined effects of surface patterning and substrate thickness maximum temperature as high as 205°C can be achieved in Pt-MG under a moderate laser excitation power of $\sim 2.8 \text{ W/mm}^2$. The flat samples require significantly higher laser power density to reach comparable temperatures because of weak absorption. The effective thermal conductivity of nanopatterned samples (nanowires + substrate) is expected to be lower than the flat samples because of enhanced boundary scattering in nanowires. This attribute, combined with the large absorption of nanowires, results in a significant temperature rise in nanopatterned MGs. Therefore, despite the thermal loss through the thick metallic substrate, the amount of heat converted is significantly larger than the heat dissipated by the sample and the temperature rises rapidly as the incident laser power is increased.

5.3.3 Finite Element Analysis of Heat Transfer Through Metallic Glass Nanowires

To further understand the photo-thermal behavior of MGs, we performed numerical simulations using COMSOL® Multiphysics software with Heat Transfer in Solids module. Heat Transfer solver interfaces define the temperature T at the boundary by the differential equation:

$$\rho C_p \frac{\partial T}{\partial t} + \nabla \cdot \mathbf{q} = Q \quad (5.1)$$

where

$$\mathbf{q} = -k\nabla T \quad (5.2)$$

and symbols ρ , C_p , \mathbf{q} , Q , and k represent the material density, the heat capacity, the heat flux, additional heat sources or sinks, and the thermal conductivity, respectively. In the

case of a stationary solver, the first term vanishes in Eq. 5.1. Plugging in Eq. 5.1 into Eq. 5.2,

$$\nabla \cdot (-k\nabla T) = Q \quad (5.3)$$

is solved by applying the appropriate boundary conditions. Eq. 5.3 is modified when convective losses are taken into consideration

$$Q_{convective} = h(T_{ext} - T) \quad (5.4)$$

where h represents the heat transfer coefficient.

Vertically aligned cylindrical nanowires with dimensions obtained from the SEM images were used in the simulations to mimic the experimental conditions. A unit cell structure comprising of a Pt-MG nanowire embedded in air was placed over a thick square Pt-MG substrate (Fig. 5.5(a)). Appropriate periodic boundary conditions were used in all simulations to emulate the periodic NWAs of the investigated samples. A two-dimensional Gaussian heat source profile was used to mimic the laser heating on the top of patterned (and flat) surfaces. Convective heat flux was also taken into consideration due to the presence of air between the nanowires. The emissivity used in the simulations was obtained by normalizing the absorption values to unity from the measured integrated diffuse reflectance of our samples (see Fig. 5.2). In our simulations, we used the MG thermal conductivity of 10 W/m.K.⁴⁴ Representative simulated temperature distributions on the top and the bottom of a single nanowire unit cell with $l/d = 10$ and $t = 50 \mu\text{m}$ (HAR-t₁) at power density $\sim 2.8 \text{ W/mm}^2$ are shown in Figs. 5.5(b) and 5.5(c), respectively. Most of the heat is transferred from the top to the bottom of the nanowire due to large thermal conductivity of MG with a corresponding temperature drop of $\sim 10\%$. Simulated temperature curves for nanopatterned (HAR-t₁, LAR-t₁, HAR-t₂, and LAR-t₂) and flat (F-t₁ and F-t₂) MG samples at different laser power densities are also shown in Fig. 5.4 for comparison with the experimental data. A good agreement between the simulations and the experiments is evident for flat and patterned samples. This indicates that the numerical analysis can be used to adequately describe the heat transport in patterned MGs as well as to predict the optimal texture and substrate thickness required to achieve the maximum temperature during photo-induced heating process.

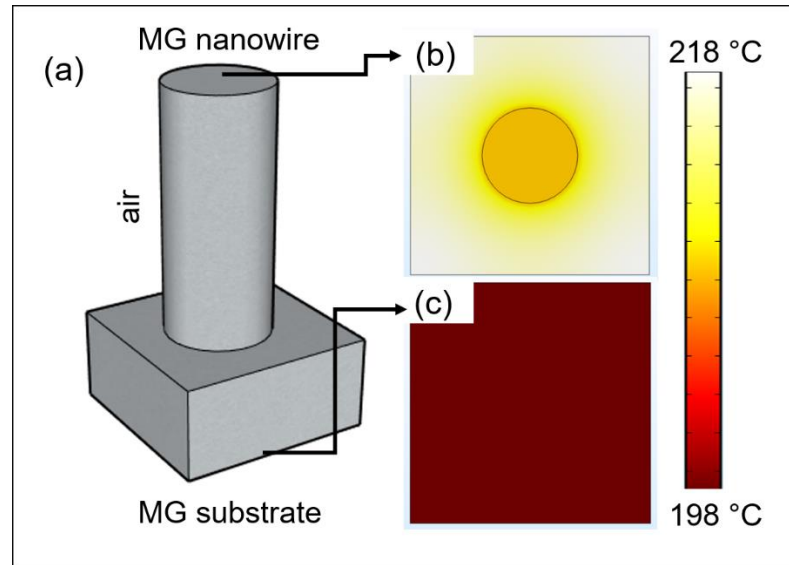


FIG. 5.5 (a) Schematic illustration of single nanowire unit cell geometry (not to scale) used in the simulations. Simulated temperature distribution of single nanowire unit cell with $l/d=10$ and $t=50 \mu\text{m}$ (HAR- t_1) at power density $\sim 2.8 \text{W}/\text{mm}^2$ (b) from the top view and (c) from the bottom view.⁴³

5.3.4 Effects of the Phase Transition on Photo-induced Temperatures

In order to investigate the effects of the atomic structure on photo-induced heating of nanopatterned MGs we fabricated amorphous and crystalline Pt-MG samples comprised of nanowires with similar aspect ratio $l/d > 10$. Laser heating experiments with power densities up to $11.5 \text{W}/\text{mm}^2$ were performed to exceed the crystallization temperature of Pt-MG.⁴⁴ Figure 5.6(a) shows the maximum photo-induced temperature rise on the surface of the amorphous and the crystalline (VHR- t) samples for different laser power densities. The maximum temperature on the crystalline sample continuously rises with increasing laser power density reaching a temperature of $\sim 557^\circ\text{C}$ at $9.1 \text{W}/\text{mm}^2$. In contrast, the amorphous sample exhibits a step-like jump in temperature above 300°C . The temperature jump originates from the amorphous to crystalline phase transition in Pt-MG.^{25,44} To verify this, we performed a second set of temperature measurements on the amorphous sample at the same spot after reaching 550°C during first experiment. As clearly shown in Fig. 5.6(a) (Exp#2), the temperature jump was no longer observed. Amorphous to crystalline transformation (devitrification) is irreversible, and therefore, the second heating curve appears smooth alike the curve for the crystalline sample. Two

heating curves measured at the same spot confirm that the step-like change in temperature of the amorphous nanopatterned Pt-MG is due to heating-induced crystallization. The crystalline state of Pt-MG has different optical (refractive index) and thermal (conductivity) properties than the amorphous state. Consequently, the first (Exp#1) and the second (Exp#2) photo-thermal temperature curves are different. It is worth noting that the as-prepared crystalline nanopatterned sample generates significantly higher heating than the amorphous counterpart exposed to the same laser flux up to the glass transition temperature of $\sim 230^{\circ}\text{C}$ (Fig. 5.6(a)). This indicates that the as-prepared crystalline sample has lower effective thermal conductivity which suggests that as prepared crystalline sample consists of higher aspect ratio nanowires. The temperature curves of two crystalline samples i.e., the as-prepared (VHR-t Crystalline) and the crystallized by laser heating (VHR-t Amorphous Exp#2) also differ due to slight change in geometry of nanowires upon laser exposure. The as-prepared sample was crystallized during thermoplastic molding where the nanowires were confined in alumina template. Therefore, the nanowire shape and size remained nearly intact during crystallization (Fig. 5.6(b)). The laser-induced heating results in slight distortion of MG nanowires above T_g due to the action of capillary stress on an unconfined state (Fig. 5.6(c)).⁴⁶ The morphological differences between two crystalline samples affect their optical absorption and thermal transport, which result in a different photo-thermal response.

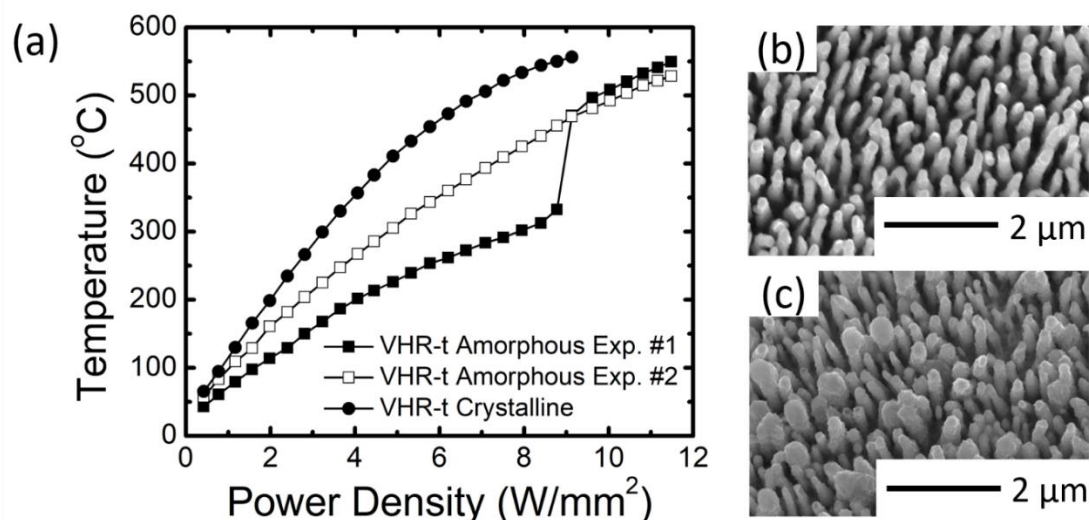


FIG. 5.6 (a) Measured maximum photo-induced temperature rise on patterned amorphous and crystalline Pt-MG (VHR-t) samples at different laser excitation power densities. SEM image of (b) the as-prepared crystalline sample (VHR-t Crystalline), and (c) the sample crystallized by photo-induced heating (VHR-t Amorphous Exp #2).⁴³

5.4 An Application of Heat Conversion: Optical Ignition of Al+CuO Thermite Powder

An important photo-thermal application is the laser induced ignition of a thermite reaction. Thermite is a mixture of metal fuel and metal oxide particles that undergo an exothermic reaction upon heating during ignition. Large heat released in the thermite reaction is utilized in a wide range of applications in defense, manufacturing, and metallurgy.^{47,48} The amount of released heat and the ignition temperature depend on the composition and the size of the thermite particles.⁴⁹ Various techniques such as flash,⁵⁰ electrical,⁵¹ mechanical,⁵² and laser stimuli⁵³ have been used to stimulate thermite ignition. Laser ignition has gained significant interest because of safety, insensitivity to environmental conditions, remotely accessible, nonintrusive and contactless heating of thermites.⁵⁴ However, high power lasers such as CO₂, excimer or Nd:YAG are required⁵⁴ to attain ignition temperatures due to poor absorption of metal particles except at the plasmon resonance. Crystallized MG nanowires are good candidates for laser ignition of thermite powders due to their ability to generate high temperatures at moderate incident laser powers

therefore enabling the use of more compact and low-cost semiconductor diode lasers for ignition.

To this end, we experimented with a thermite mixture of stoichiometrically balanced nano-sized Al (~100 nm) and CuO (~25-50 nm) powders that ignite at 550°C with an exothermic heat of 4.1 kJ/g.⁵⁵ A homogeneous mixture was prepared by suspending the powders in isopropyl alcohol carrier fluid followed by sonication for 1 hr. The sonication process breaks up agglomerates and provides more homogeneous mixing between fuel and oxidizer powders. The solution was spin coated on crystalline Pt-MG nanowires and dried in air to form a conformal thermite layer. Three coats were applied to achieve a semi-continuous thermite layer necessary for propagation of the reaction front upon ignition. As shown in Fig. 5.7(a), some sections of the MG nanowires were not covered with thermite to allow absorption of laser by the nanowires. The same continuous wave NIR semiconductor laser diode ($\lambda = 980$ nm) employed in the thermography experiments, but with a reduced spot size (spot size diameter 50-70 μm), was used for the ignition tests (Fig. 5.7(b)). Thermite powder coated on a glass slide was also exposed to the same laser conditions for comparison. The thermite powder coated onto MG NWAs ignited at ~ 12 W/mm² power density and the ignition resulted in formation of a hole in the MG NWA sample due to a large exothermic heat generated during the ignition process (Fig. 5.7(a)). As shown by the still images (Fig. 5.7(b)) captured from the video streaming using a CCD camera, the ignition started at about 8 ms after laser exposure. The reaction products were reclaimed, analyzed using EDX, and composed of aluminum oxide (Al₂O₃) and copper (Cu) were consistent with the balanced chemical reaction.



In contrast, the ignition was not observed for the thermite mixture on the glass slide, even up to an order of magnitude higher laser power densities. Non-ignition is attributed to the significantly less absorption and lower temperature of the unpatterned substrate that did not provide sufficient thermal stimuli to ignite the thermite powder compared to the crystallized MG nanowires (i.e., $\sim 95\%$ laser power absorption) in the NIR. In addition to the large absorption, the MG nanowire architecture results in fast temperature rise due to minimal thermal losses through lateral heat conduction (see Fig. 5.5). Thus, the ignition temperature of the thermite can be reached at lower incident laser powers using MG

NWA, eliminating the need for bulky and costly high-power lasers typically used for ignition.

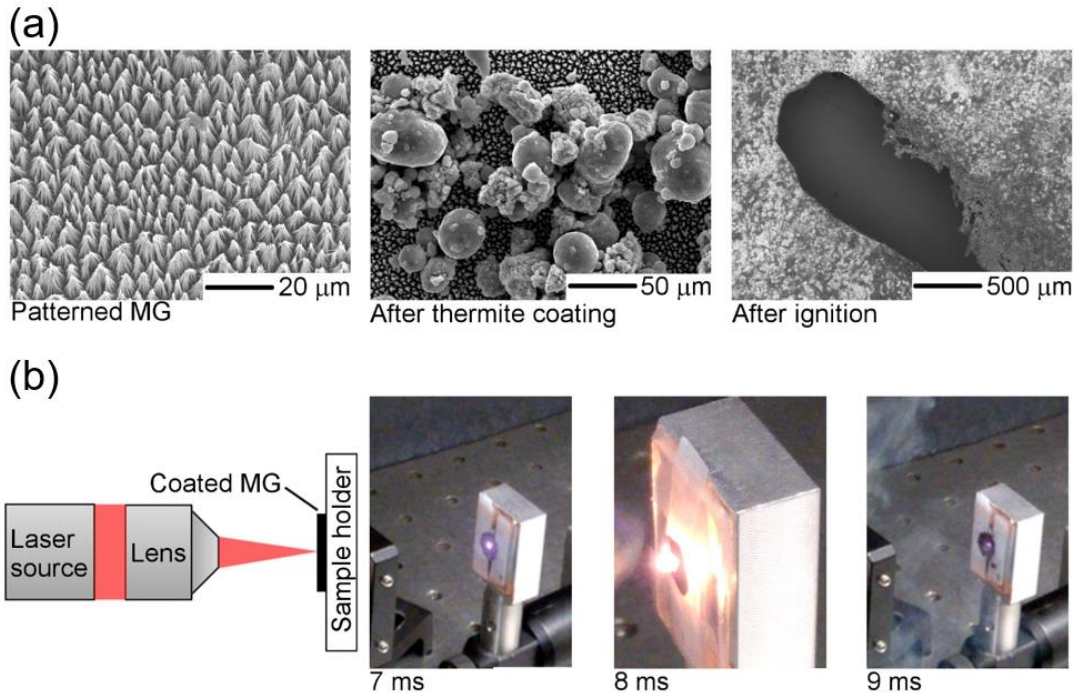


FIG. 5.7 (a) SEM images of nano-patterned Pt-MG in the as-prepared state, after coating with thermite mixture, and after laser ignition of thermite. (b) Schematic illustration of laser ignition setup and still images captured at different times from the video recording obtained with a laser power density $\sim 12 \text{ W/mm}^2$.^{2,43}

5.5 Conclusions

In this chapter, we investigated the influence of surface texture, substrate thickness, and structural state of MG samples for achieving high temperatures upon NIR laser illumination. IR thermography measurements show that high photo-thermal temperatures can be achieved by reducing the substrate thickness and by increasing the length of surface nanowires. The effect of thickness is attributed to change in the thermal resistance of MG substrate. Longer nanowires generate higher temperature as a result of enhanced optical absorption and confinement of heat in nanoscale channels.

Experimental results were verified by finite element analysis of the heat transport, which can be used for optimization of surface texture for a desirable photo-thermal outcome. We further showed that the phase transformation of MG nanowires from amorphous to

crystalline state can be achieved by photo-induced heating. Evidently, the phase change in MG nanowires is not a limiting factor for photo-thermal applications. Our results suggest that MG nanowires can be utilized in photo-thermal applications due to their high absorption and heat transfer capabilities. We demonstrate one such application where a thermite mixture was ignited at significantly lower laser flux using MG nanowires than the bare sample.

CHAPTER 6

DIELECTRIC PROPERTIES OF CRYSTALLINE AND AMORPHOUS METALLIC GLASSES

6.1 Introduction

The absorption properties of a material depends on the material composition as well as the surface topology. The interaction of light of different wavelengths with the material can be described by the dispersion relations. Spectroscopic Ellipsometry is a well known method to obtain the material-dependent dispersion relation of a given material. In Chapter 2, we have investigated the effects of surface topology, i.e. the dependence of absorption on the aspect ratio of the metallic glass nanowires in the amorphous state, with diffuse reflectance measurements and Rigorous Coupled Wave Analysis (RCWA) simulations. We have briefly mentioned the material dependent dispersion relation among other parameters required as an input for RCWA analysis. However, the wavelength dispersion of the index of refraction ($n(\lambda)$) and the extinction coefficient ($k(\lambda)$) of platinum based metallic glasses (Pt-MGs) have not been explicitly presented. In this chapter, we report the optical constants of Pt-MGs in amorphous and crystalline states obtained from the Spectroscopic Ellipsometry (SE) measurements.

We showed that, although similar in trend, the dispersion relations of amorphous and crystalline Pt-MGs exhibit distinct values for n and k at each state. The ability to distinguish between amorphous and crystalline states can be potentially utilized as a complementary optical procedure to the existing methods such as differential scanning calorimetry (DSC) and X-ray diffraction.

6.2 Experimental Details

6.2.1 *Sample Preparation and Crystallization*

Unpatterned amorphous wafer of Pt-MG investigated in this study was synthesized by water quenching as described in the previous chapters. Amorphous Pt-MG sample was crystallized by isothermally heating it into the super cooled liquid region (above the glass

transition temperature $T_g \sim 230^\circ\text{C}$).^{25,44} Complete crystallization of the annealed sample was verified from DSC measurements that are not presented here. An example of the time-temperature-transition (TTT) diagram for the Pt-based metallic glass is given in Figure 6.1.⁴⁴ Evidently, how fast the phase transition from amorphous to crystalline occurs depends on the onset crystallization temperature in the super cooled liquid region. As the onset temperature of crystallization decreases, longer times are required for the completion of crystallization process throughout the material.

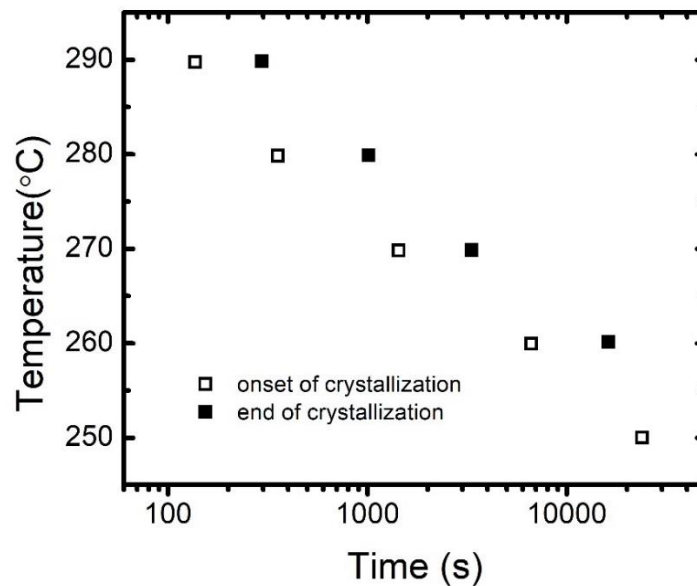


FIG. 6.1 Time-Temperature-Transition diagram for $\text{Pt}_{57.5}\text{Cu}_{14.7}\text{Ni}_{5.3}\text{P}_{22.5}$ in the super cooled liquid region. Open and closed squares represent the onset and end of crystallization, respectively. (Adapted from Reference [44])

6.2.2 Spectroscopic Ellipsometry

All our SE measurements were obtained using a Horiba Jobin Yvon UVISSEL Ellipsometer (spectral range 190-2100 nm). Light emitted from a Xenon lamp at a 70° incident angle is collimated, transmitted through a linear polarizer, and directed to the surface of the sample to be investigated. Incident and reflected electric fields can be written in terms of the perpendicular (p polarization) and the parallel component (s polarization) of the polarized incident light with respect to the incident plane as

$$\vec{E}_i = E_{i0} (\hat{s} + \hat{p})/\sqrt{2} \quad (6.1)$$

$$\vec{E}_r = E_{r0} (r_s e^{i\delta_{rs}} \hat{s} + r_p e^{i\delta_{rp}} \hat{p})/\sqrt{2} \quad (6.2)$$

After the beam is reflected from the sample surface, both parallel and perpendicular components are changed in phase and amplitude as indicated in Eq. 6.2. The beam is then transmitted through a photoelastic modulator (PEM) where a time varying phase shift is introduced (Eq. 6.3), followed by an analyzer, and finally directed to different photodetectors that cover from UV to near-infrared spectral regions. The intensity of the reflected beam, I , and the ratio of complex Fresnel reflection coefficients, r_p/r_s , are given by the Equations 6.4 and 6.5, respectively.

$$\vec{E}_r = E_{r0} (r_s e^{i\delta_{rs}} \hat{s} + r_s e^{i\delta_{rp} + i\delta_o(\sin\omega_o t)} \hat{p})/\sqrt{2} \quad (6.3)$$

$$I \propto |\vec{E}_r|^2 \propto (r_s + r_p)^2 (1 \pm \text{Const.} \cos \Delta) \quad (6.4)$$

$$\rho = \frac{|r_p|}{|r_s|} = \tan \Psi e^{i\Delta} \quad (6.5)$$

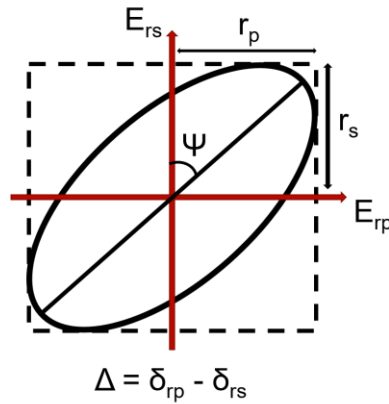


FIG. 6.2 Schematic representation of the elliptical polarization state showing the electric field amplitudes (E_{rp} and E_{rs}) and the ellipsometry angles Δ and Ψ .

The schematic illustration of the elliptically polarized reflected beam that is transmitted to the analyzer is shown in Fig. 6.2. Ellipsometer angles Δ and Ψ are related to the phase difference and reflection coefficients along p and s directions by Eqs. 6.6 and 6.7, respectively. Measured intensities related to the the second (I_s) and the first harmonic (I_c)

of the reflected beam can be written in terms of the ellipsometer angles Δ and Ψ using Equations 6.8 and 6.9.

$$\Psi = \tan^{-1} \frac{|r_p|}{|r_s|} \quad (6.6)$$

$$\Delta = \delta_{rp} - \delta_{rs} \quad (6.7)$$

$$I_s = \sin 2\Psi \sin \Delta \quad (6.8)$$

$$I_c = \sin 2\Psi \cos \Delta \quad (6.9)$$

In order to interpret the acquired data, a physical model of the material composition and structure is required. Various dispersion functions such as Tauch-Lorentz, Lorentz oscillator, Cauchy, Sellmeier, and Drude can be employed in a model based on the properties of the material that is investigated. After the model is selected, the measured intensities I_s and I_c are fitted in order to extract the optical constants. For SE modelling of both amorphous and crystalline metallic glasses, we adopted the Drude model using the ellipsometric analysis software package Horiba Deltapsi-2. Drude's model for the complex dielectric function $\varepsilon(\omega)$ as a function of frequency is given by

$$\varepsilon(\omega) = \varepsilon_\infty - \frac{\omega_p^2}{\omega^2 + i\omega\Gamma_D} \quad (6.10)$$

where ε_∞ is the dielectric constant in the high frequency limit, ω_p is the plasma frequency, Γ_D is the free electron damping factor, and $\varepsilon(\omega) = [n(\omega) + ik(\omega)]^2$. The quality of the fit is provided by the parameter χ^2 which is an indicator of the agreement between the simulation (via the least squares fitting method) and the experimental data.

6.3 Results and Discussion

After measuring the parameters I_s and I_c of the Pt-MG in the amorphous state, the sample was crystallized at $T=280^\circ\text{C}$ for ~15 minutes. A second SE measurement was performed on the same sample in the crystalline state (after crystallization). The XRD patterns of the Pt-MG in the crystalline and amorphous states are shown in Figure 6.3 (a) and (b), respectively.⁵⁶ The Pt-MG in the amorphous state exhibits a broad peak which is a signature of the amorphous structure. In contrast, the XRD spectrum of the crystalline

sample shown in Fig. 6.3 (a) revealed multiple narrow peaks corresponding to different crystalline phases of the Pt-MG which occurred during the crystallization process.

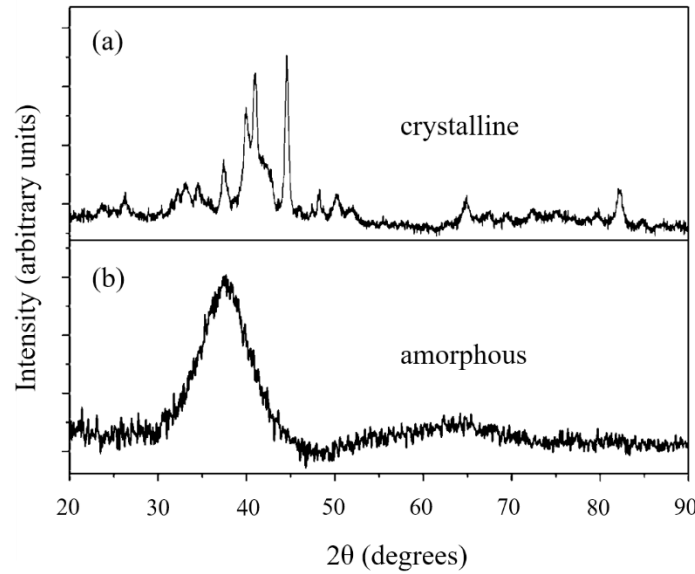


FIG. 6.3 XRD patterns of the Pt-MG in (a) the crystalline state, and (b) the amorphous state, respectively. (Adapted from Reference [56])

Using the Drude model, the parameters for amorphous and crystalline states were determined as $\varepsilon_{\infty} = 1.2$ eV and 1.5 eV, $\omega_p = 22$ eV and 25 eV, and $\Gamma_D = 15.2$ eV and 13.5 eV, respectively. The plasma frequencies for the amorphous and the crystallized samples were found to be significantly higher than most elementary metals.^{57,58} This indicates that Pt-based alloys can be potentially utilized in the extreme UV applications as reflectors, for instance. The large Drude damping factors stem from a decrease in electron relaxation time in amorphous and crystalline alloys.^{27,58}

Measured and fitted I_s and I_c parameters for Pt-MG samples in amorphous and crystalline states as a function of wavelength are shown in Figure 6.4 (a) and (b), respectively. Corresponding standard deviations of the fits are determined to be $\chi^2 = 0.038$ and 0.036 for amorphous and crystalline states, indicating a good agreement between the model and the SE measurements.

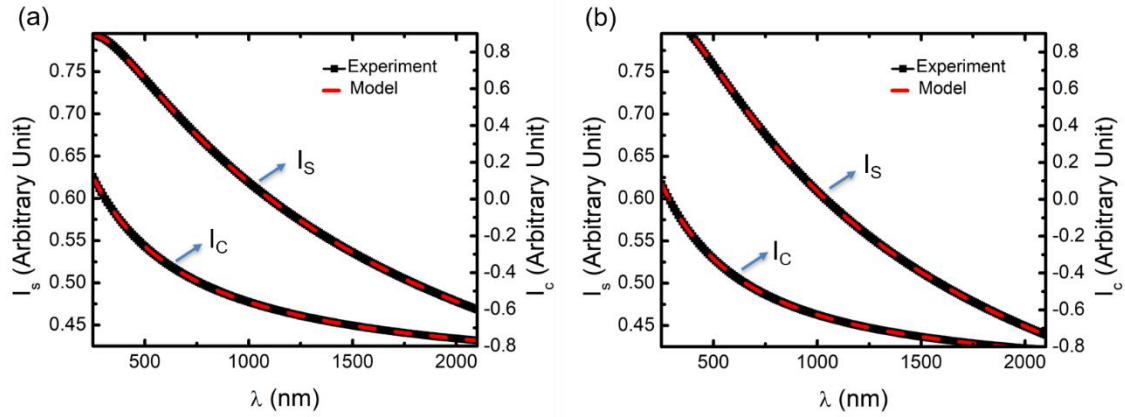


FIG. 6.4 Measured and fitted I_s and I_c parameters as a function of wavelength for Pt-MG sample in (a) the amorphous state, and (b) the crystalline state.

The wavelength dispersion of n and k for both amorphous and crystalline Pt-MGs are shown in Figure 6.4. Both index of refraction (n) and extinction coefficient (k) for amorphous and crystalline Pt-MGs exhibited a featureless monotonic increase in the investigated wavelength range. The transition from amorphous to crystalline state results in structural heterogeneity and periodicity. Thus, higher n and k values observed in the crystalline state are likely to stem from the higher mass density due to crystallization.

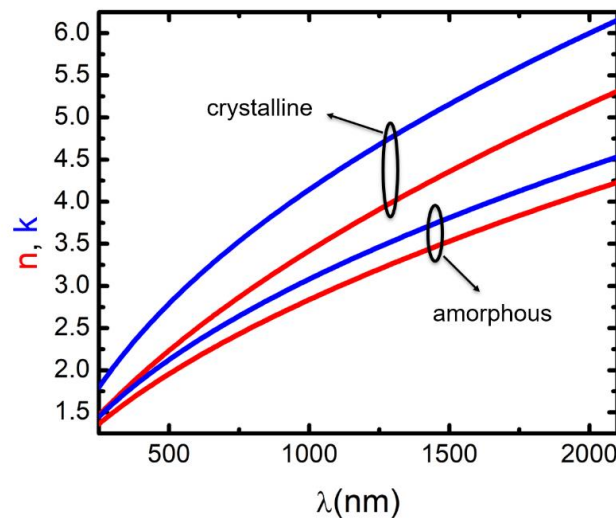


FIG. 6.5 Index of refractions (n) and extinction coefficients (k) as a function of wavelength for amorphous and crystalline Pt-MG.

6.4 Conclusions

In this chapter, we investigated the wavelength-dependent dispersion relations of Pt-MG samples in the amorphous and crystalline states using spectroscopic ellipsometry measurements. The determined higher values of the index of refraction and the extinction coefficient for MG in the crystalline phase when compared to the amorphous one, are attributed to the higher material density in the crystalline state as a result of its periodicity and long-range order. The material homogeneity that the phase transition enables, results in closely packing of the different crystalline phases within the material, thus increasing the index of refraction of the investigated Pt-MG alloys. We anticipate that the SE method can be potentially utilized to further understand the crystallization formation in MGs.

CHAPTER 7

CONCLUSIONS

In this dissertation, we have explored the optical, thermal, and crystallization properties of Pt-based metallic glasses with different topological parameters. First, we have investigated the absorption characteristics of both unpatterned MGs and patterned MG-NWAs with different length-to-diameter aspect ratios. Diffuse reflectance measurements at $\lambda=980$ nm and RCWA simulations revealed a significant decrease in reflectivity as the aspect ratio of the MG-NWs is increased. This reduction in diffuse reflectance is attributed to the decrease in surface-to-volume ratio resulting in multiple absorption events that enhance the overall absorption. We have also explored the wavelength dependence of the diffuse reflection at other wavelengths ($\lambda=532$ nm and 1560 nm) and determined that it increases as the wavelength of the illumination is increased. Despite the observed decrease in absorption at higher wavelengths, we demonstrated that it is possible to further reduce the reflectance by bundling the vertically aligned MG-NWAs by placing the sample in a liquid solution. Our RCWA simulations revealed that an 80% reduction in diffuse reflectance can be achieved upon increasing the number of nanowires in a bundle to ~ 12 from the initial vertically aligned arrangement.

Furthermore, we have explored the scattering properties of MG-NWs using far-field speckle image analysis. Using a Matlab® program that is based on statistical image analysis, we determined the distinct features of speckle images that were obtained from MG-NWs with different aspect ratios, amorphicity and crystallinity. We showed that the statistical parameters that correspond to these features can be implemented in various machine learning algorithms such as lazy IBk, Naïve Bayes, Logistic Regression, and SMO. Evidently, all these classifier algorithms can be used to distinguish one sample from another with $\sim 100\%$ accuracy. The ability to recognize a certain type of sample from an ensemble with similar properties based on its speckle image enabled the realization of a speckle analysis-based method for characterization of the surface topology and the structural state of the MGs.

In addition to low reflectance, we demonstrated distinct heat localization and significant temperature rise on Pt-MGs illuminated by an infrared laser source. This is attributed to

nanowire topology that results in lower effective thermal conductivity in the lateral directions. Marked temperature contrast between illuminated and non-illuminated areas even under low optical power excitation conditions enabled the generation of legible photo-induced thermal patterns on textured metallic glass surfaces. We anticipate that the heat localization that MG-NWAs enable can potentially be utilized in photo-thermal-electric energy conversion applications, as broad-band absorbers, and for mid-IR cipherring, steganography, tagging and tracking.

In order to further optimize the heat generation, we studied the effect of topological parameters of the Pt-MG nanowire samples such as the wire diameter, the periodicity, the length, and the substrate thickness as well as the effects of crystallinity on the photo-induced temperatures. Our thermography measurements and heat transport simulations revealed the relation between optical absorption and localized heat conversion.

Nanowires with higher aspect-ratios result in higher temperatures due to enhanced optical absorption and efficient confinement of heat within the periodic nano structures. The observed significant reduction in photo-induced temperatures on the samples with thicker substrates is attributed to the increase in thermal resistance. IR thermography measurements obtained from very high aspect ratio samples ($l/d > 20$) revealed that the temperatures above $\sim 500^\circ\text{C}$ can be rapidly induced on the NWAs. The ability to generate temperatures greater than the glass transition temperature for Pt-MGs ($\sim 230^\circ\text{C}$) indicates that the phase transition from amorphous to crystalline state is not a limiting factor for potential photo-thermal applications. In order to verify this point, we utilized a high aspect ratio Pt-MG NW sample as the supporting substrate for Al+CuO thermite powder in laser-ignition experiments. We showed that the laser flux that is required for ignition can be significantly reduced with the use of Pt-MG NWAs when compared to the powder pellets alone. This is attributed to the rapid generation, localization and conduction of heat that the Pt-MG NW structure enables.

Lastly, we explored the effects of structural state (amorphous and crystalline) on the optical characteristics of unpatterned Pt-based MGs. The wavelength dependent dispersion relations of amorphous and crystalline samples were obtained using spectroscopic ellipsometry. The larger n and k values determined for samples in the crystalline state, in comparison to the amorphous counterpart, stem from the higher

material density which is a result of the reduction in volume with the introduction of long-range structural order upon the phase transition. We anticipate that an optical characterization method based on spectroscopic ellipsometry can be used in the classification of amorphous and crystallinity states of unpatterned MGs, complementary to the existing methods such as X-ray diffraction and differential scanning calorimetry.

7.1 List of Publications

- **C Uzun**, C Meduri, N Kahler, LG de Peralta, M Pantoya, G Kumar, AA Bernussi, “Photoinduced heat conversion enhancement of metallic glass nanowire arrays” *Journal of Applied Physics* 125 (1), 015102.
 - **C Uzun**, N Kahler, LG de Peralta, G Kumar, AA Bernussi, “Photo-induced heat localization on nanostructured metallic glasses” *Journal of Applied Physics* 122 (9), 094306.
 - **C Uzun**, N Kahler, LG de Peralta, G Kumar, AA Bernussi, “Programmable infrared steganography using photoinduced heating of nanostructured metallic glasses” In 2017 Conference on Lasers and Electro-Optics (CLEO), pp.1-2. IEEE, 2017.
 - Z Hu, **C Uzun**, Z Dong, W Li, AA Bernussi, G Kumar, “Elastocapillary bundling of high aspect-ratio metallic glass nanowires” *Applied Physics Letters* 111 (2), 023107.
 - **C Uzun**, C Meduri, G Kumar, AA Bernussi, “Ellipsometric analysis of crystallinity of metallic glasses”, in preparation.
 - **C Uzun**, M Uzun, C Meduri, G Kumar, AA Bernussi, “Speckle image analysis of metallic glass scatterers via classifier algorithm”, in preparation.
-
- H Algasham, H Farooq, **C Uzun**, S Skinner-Ramos, AA Bernussi, LG de Peralta, “Scanning diffracted-light photography using white-light and thermal radiation sources” *Applied Optics* 57 (34), 9997-10003.

REFERENCES

1. Aliev, A. E., Gartstein, Y. N. & Baughman, R. H. Mirage Effect from Thermally Modulated Transparent Carbon Nanotube Sheets. *Nanotechnology* **22**, 10 (2011).
2. Hogan, N. J. *et al.* Nanoparticles Heat through Light Localization. *Nano Lett.* **14**, 4640–4645 (2014).
3. Iyengar, V. V., Nayak, B. K. & Gupta, M. C. Optical Properties of Silicon Light Trapping Structures for Photovoltaics. *Sol. Energy Mater. Sol. Cells* **94**, 2251–2257 (2010).
4. Ghasemi, H. *et al.* Solar Steam Generation by Heat Localization. *Nat. Commun.* **5**, 4449 (2014).
5. Pop, E., Sinha, S. & Goodson, K. E. Heat Generation and Transport in Nanometer-Scale Transistors. *Proc. IEEE* **94**, 1587–1601 (2006).
6. Brown, M. S. & Arnold, C. B. Laser Precision Microfabrication. in *Springer Series in Materials Science* **135**, 91–120 (2010).
7. Lee, Y. J., Ruby, D. S., Peters, D. W., McKenzie, B. B. & Hsu, J. W. P. ZnO Nanostructures as Efficient Antireflection Layers in Solar Cells. *Nano Lett.* **8**, 1501–1505 (2008).
8. Jiang, T., Lee, E., Young, M. & Luo, T. Nanostructure-Enabled Significant Thermal Transport Enhancement across Solid Interfaces. in *15th IEEE ITherm Conference* 652–656 (2016).
9. Zhu, J. *et al.* Optical Absorption Enhancement in Amorphous Silicon Nanowire and Nanocone Arrays. *Nano Lett.* **9**, 279–282 (2009).
10. Quijada, M. A., Hagopian, J. G., Getty, S., Kinzer, Jr., R. E. & Wollack, E. J. Hemispherical Reflectance and Emittance Properties of Carbon Nanotubes Coatings at Infrared Wavelengths. *SPIE Cryog. Opt. Syst. Instruments XIII* **8150**, 815002-815002–11 (2011).
11. Yang, R., Chen, G. & Dresselhaus, M. S. Thermal Conductivity of Simple and Tubular Nanowire Composites in the Longitudinal Direction. *Phys. Rev. B* **72**, 1–7 (2005).
12. Zhou, W. & Wang, L. Z. *Three-Dimensional Nanoarchitectures*. (Springer, 2000).
13. Baughman, R. H., Zakhidov, A. A. & De Heer, W. A. Carbon nanotubes - The route toward applications. *Science (80-.)*. **297**, 787–792 (2002).
14. Mizuno, K. *et al.* A black body absorber from vertically aligned single-walled carbon nanotubes. *Proc. Natl. Acad. Sci. U. S. A.* **106**, 6044–6047 (2009).
15. Yang, Z. P., Ci, L., Bur, J. A., Lin, S. Y. & Ajayan, P. M. Experimental observation of an extremely dark material made by a low-density nanotube array. *Nano Lett.* **8**, 446–451 (2008).
16. Yaghoobi, P., Moghaddam, V. M. & Nojeh, A. “ Heat Trap ”: Light-induced Localized Heating and Thermionic Electron Emission from Carbon Nanotube

- Arrays. *Solid State Commun.* **151**, 1105–1108 (2011).
17. Roder, P. B., Smith, B. E., Davis, E. J. & Pauzauskie, P. J. Photothermal heating of nanowires. *J. Phys. Chem. C* **118**, 1407–1416 (2014).
 18. Walia, J. *et al.* Enhanced photothermal conversion in vertically oriented gallium arsenide nanowire arrays. *Nano Lett.* **14**, 5820–5826 (2014).
 19. M. S. Dresselhaus X. Sun, Z. Zhang, S. B. Cronin, T. Koga, J. Y. Ying, G. Chen, G. D. THE PROMISE OF LOW-DIMENSIONAL THERMOELECTRIC MATERIALS. *Microscale Thermophys. Eng.* **3**, 89–100 (1999).
 20. Barako, M. T. *et al.* Thermal Conduction in Vertically Aligned Copper Nanowire Arrays and Composites. *ACS Appl. Mater. Interfaces* **7**, 19251–19259 (2015).
 21. Choi, S. M., Kim, J. H., Jung, J. Y., Yoon, E. Y. & Kim, W. B. Pt nanowires prepared via a polymer template method: Its promise toward high Pt-loaded electrocatalysts for methanol oxidation. *Electrochim. Acta* **53**, 5804–5811 (2008).
 22. Paulo, A. S. *et al.* Mechanical elasticity of single and double clamped silicon nanobeams fabricated by the vapor-liquid-solid method. *Appl. Phys. Lett.* **87**, 1–4 (2005).
 23. Li, A. W. Z. *et al.* Large-Scale Synthesis of Aligned Carbon Nanotubes. *Am. Assoc. Adv. Sci.* **274**, 1701–1703 (2016).
 24. Kumar, G., Tang, H. X. & Schroers, J. Nanomoulding with Amorphous Metals. *Nature* **457**, 868–872 (2009).
 25. Kumar, G., Desai, A. & Schroers, J. Bulk Metallic Glass: The Smaller the Better. *Adv. Mater.* **23**, 461–476 (2011).
 26. Schroers, J., Kumar, G., Hodges, T. M., Chan, S. & Kyriakides, T. R. Bulk Metallic Glasses for Biomedical Applications. *JOM* **61**, 21–29 (2009).
 27. Tarigan, H. J., Kahler, N., Ramos, N. S., Kumar, G. & Bernussi, A. A. Low Reflectance of Nano-patterned Pt-Cu-Ni-P Bulk Metallic Glass. *Appl. Phys. Lett.* **107**, (2015).
 28. Hu, Z. *et al.* Elastocapillary bundling of high aspect-ratio metallic glass nanowires. *Appl. Phys. Lett.* **111**, (2017).
 29. Katiyar, A. K., Mukherjee, S., Zeeshan, M., Ray, S. K. & Raychaudhuri, A. K. Enhancement of Efficiency of a Solar Cell Fabricated on Black Si Made by Inductively Coupled Plasma–Reactive Ion Etching Process: A Case Study of a n-CdS/p-Si Heterojunction Cell. *ACS Appl. Mater. Interfaces* **7**, 23445–23453 (2015).
 30. Lin, H. *et al.* Developing controllable anisotropic wet etching to achieve silicon nanorods, nanopencils and nanocones for efficient photon trapping. *J. Mater. Chem. A* **1**, 9942–9946 (2013).
 31. HIRAKAWA, Y. & MATSUKI, Y. Living Plant Observation by a Laser Speckle Microscopy. *Rev. Laser Eng.* **36**, 1355–1357 (2008).
 32. Balamurugan, R. Laser Speckle Image Processing. *Int. J. Comput. Sci. Eng.*

- Technol.* **7**, 163–166 (2016).
33. Ohlídal, M., Unčovský, M., Ohlídal, I. & Franta, D. Determination of the basic parameters characterizing the roughness of metal surfaces by laser light scattering. *J. Mod. Opt.* **46**, 279–293 (1999).
 34. Dunn, A. K. Laser Speckle Contrast Imaging of Cerebral Blood Flow. *Ann. Biomed. Eng.* **40**, 367–377 (2012).
 35. Valent, E. & Silberberg, Y. Scatterer recognition via analysis of speckle patterns. *Optica* **5**, 204 (2018).
 36. Systems, C. Scatterer recognition via analysis of speckle patterns : supplementary material. **0**, (2018).
 37. Hall, M. *et al.* The WEKA Data Mining Software: An Update. *SIGKDD Explor. Newsl.* **11**, 10–18 (2009).
 38. Aha, D. W., Kibler, D. & Albert, M. K. Instance-based learning algorithms. *Mach. Learn.* **6**, 37–66 (1991).
 39. Zeng, Z.-Q., Yu, H.-B., Xu, H.-R., Xie, Y.-Q. & Gao, J. Fast training support vector machines using parallel sequential minimal optimization. in *2008 3rd international conference on intelligent system and knowledge engineering* **1**, 997–1001 (IEEE, 2008).
 40. John, G. H. & Langley, P. Estimating continuous distributions in Bayesian classifiers. *arXiv Prepr. arXiv1302.4964* (2013).
 41. Le Cessie, S. & Van Houwelingen, J. C. Ridge estimators in logistic regression. *J. R. Stat. Soc. Ser. C (Applied Stat.)* **41**, 191–201 (1992).
 42. Uzun, C., Kahler, N., De Peralta, L. G., Kumar, G. & Bernussi, A. A. Photo-induced-heat localization on nanostructured metallic glasses. *J. Appl. Phys.* **122**, 1–6 (2017).
 43. Uzun, C. *et al.* Photoinduced heat conversion enhancement of metallic glass nanowire arrays. *J. Appl. Phys.* **125**, 15102 (2018).
 44. Schroers, J. & Johnson, W. L. Highly processable bulk metallic glass-forming alloys in the Pt-Co-Ni-Cu-P system. *Appl. Phys. Lett.* **84**, 3666–3668 (2004).
 45. Cheng, Z., Liu, L., Xu, S., Lu, M. & Wang, X. Temperature Dependence of Electrical and Thermal Conduction in Single Silver Nanowire. *Sci. Rep.* **5**, (2015).
 46. Kumar, G. & Schroers, J. Write and erase mechanisms for bulk metallic glass. *Appl. Phys. Lett.* **92**, 90–93 (2008).
 47. Stacy, S. C. & Pantoya, M. L. Laser ignition of nano-composite energetic loose powders. *Propellants, Explos. Pyrotech.* **38**, 441–447 (2013).
 48. Hunt, E. M. & Pantoya, M. L. Ignition dynamics and activation energies of metallic thermites: From nano- to micron-scale particulate composites. *J. Appl. Phys.* **98**, (2005).
 49. Walter, K. C., Aumann, C. E., Carpenter, R. D., O’Neill, E. H. & Pesiri, D. R.

- Energetic Materials Development at Technanogy Materials Development. *MRS Proc.* **800**, AA1.3 (2003).
50. Ohkura, Y., Rao, P. M. & Zheng, X. Flash ignition of Al nanoparticles: Mechanism and applications. *Combust. Flame* **158**, 2544–2548 (2011).
 51. Weismiller, M. R., Malchi, J. Y., Yetter, R. A. & Foley, T. J. Dependence of flame propagation on pressure and pressurizing gas for an Al/CuO nanoscale thermite. *Proc. Combust. Inst.* **32 II**, 1895–1903 (2009).
 52. Barbee Jr, T. W., Gash, A. E., Satcher Jr, J. H. & Simpson, R. L. *Nanotechnology based environmentally robust primers*. (Lawrence Livermore National Lab., CA (US), 2003).
 53. Granier, J. J. & Pantoya, M. L. Laser ignition of nanocomposite thermites. *Combust. Flame* **138**, 373–383 (2004).
 54. De Yong, L., Nguyen, T. & Waschl, J. *Laser Ignition of Explosives, Pyrotechnics and Propellants: A Review*. (DEFENCE SCIENCE AND TECHNOLOGY ORGANIZATION CANBERRA (AUSTRALIA), 1995).
 55. Petrantoni, M. *et al.* Synthesis process of nanowired Al/CuO thermite. *J. Phys. Chem. Solids* **71**, 80–83 (2010).
 56. Mridha, S., Jaeger, D. L., Arora, H. S., Banerjee, R. & Mukherjee, S. Atomic distribution in catalytic amorphous metals. *J. Nanomater.* **2015**, (2015).
 57. Blaber, M. G., Arnold, M. D. & Ford, M. J. A review of the optical properties of alloys and intermetallics for plasmonics. *J. Phys. Condens. Matter* **22**, (2010).
 58. Tarigan, H. J. Ultra-low optical scattering with nano-structured bulk metallic glasses. *Ultra-low Opt. Scatt. with nano-structured bulk Met. Glas.* (2016).